Chapter 10
Electrospun Nanostructured Iron Oxides for High-Performance Lithium Ion Batteries

Neethu T. M. Balakrishnan, Akhila Das, N. S. Jishnu, M. A. Krishnan, Sabu Thomas, M. J. Jabeen Fatima, Jou-Hyeon Ahn, and Raghavan Prasanth

10.1 Introduction

The rechargeable Li-ion battery (LIB) has attracted intensive research interest due to their large spectrum of applications as energy storage devices for electric, electric/hybrid electric vehicles, and intermittent renewable energy sources [1–5]. The LIB is referred to as a rocking-chair battery, because Li^+-ions "rock" back and forth between the anode and the cathode during cycling and they possess high energy and power densities, no memory effect and long cycle life. The current generation commercial LIBs are utilizing the electrode materials, which could store Li^+-ions

N. T. M. Balakrishnan · A. Das · M. J. Jabeen Fatima · R. Prasanth
Department of Polymer Science and Rubber Technology, Cochin University of Science and Technology (CUSAT), Cochin 682022, India
e-mail: jabeen@cusat.ac.in

N. S. Jishnu
Rubber Technology Centre, Indian Institute of Technology-Kharagpur (IIT-KGP), Kharagpur, West Bengal 721302, India

M. A. Krishnan
Department of Mechanical Engineering, Amrita Vishwa Vidyapeetham, Amritapuri, India

Department of Electrical Engineering, Pennsylvania State University, 311, Electrical Engineering East Building, University Park, PA 16802, USA

S. Thomas
School of Chemical Sciences, Mahatma Gandhi University, Athirampuzha, Kerala 686560, India

J.-H. Ahn (✉) · R. Prasanth (✉)
Department of Materials Engineering and Convergence Technology, Gyeongsang National University, 501 Jinju-daero, Jinju 52828, Republic of Korea
e-mail: jhahn@gnu.ac.kr

R. Prasanth
e-mail: prasanth@cusat.ac.in

N. T. M. Balakrishnan and R. Prasanth (eds.), *Electrospinning for Advanced Energy Storage Applications*, Materials Horizons: From Nature to Nanomaterials,
https://doi.org/10.1007/978-981-15-8844-0_10

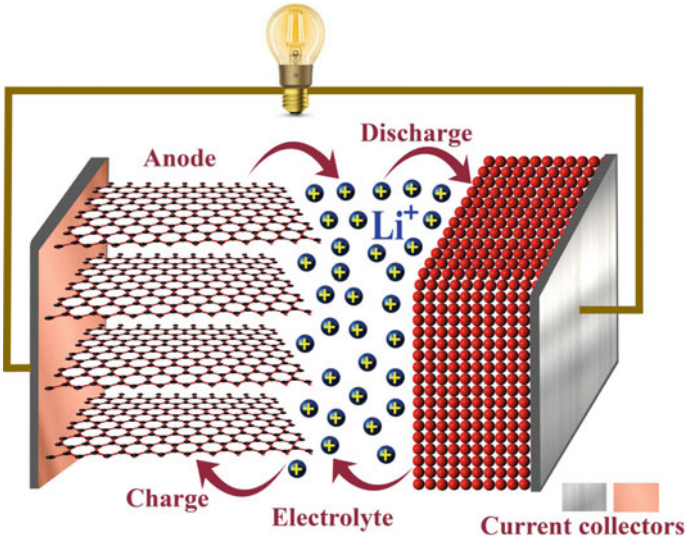

Fig. 10.1 Schematic representation and operating principle of lithium ion batteries

by insertion between their structural layers during charging and extracted out from the layers during discharging (Fig. 10.1) without any significant structural change leading to excellent cycling performance. In recent years, globally great efforts have been paid by the researchers and battery technologists to develop and design high-performance electrode materials in terms of energy density, cycling stability and rate capability. Among different classes of anode materials such as intercalation, conversion reaction, alloying/de-alloying reaction-type materials, transition metal oxides, Co_3O [6–10], FeOx [11–17], TiO_2 [18, 19], MnO_2 [20–22], and SnO_2 [23–25], iron oxide micro-/nanomaterials, such as hematite (α-Fe_2O_3) [26–28] and magnetite (Fe_3O_4) [29–31], have been extensively studied as potential electrode materials in LIBs. Iron oxide is popular in their higher theoretical capacities (1004 mAh g^{-1} for α-Fe_2O_3 and 924 mAh g^{-1} for Fe_3O_4), has low toxicity, and is economically viable.

In spite of their lower cost and better safety, the capacity retention of Fe_2O_3/Fe_3O_4 remains a major drawback, due to the huge volumetric expansion/contraction during the lithiation/delithiation process which ultimately leads to pulverization of the electrode from the current collector, resulting in loss of electrical contact and loss of morphological structure of the active material [32]. The electrochemical performance is highly dependent on their diverse morphologies and micro-/nanostructure of an anode material [33–37] The confining dimension effect and high surface area of the nanostructured materials lead to the short lithium diffusion lengths and increased active sites for Li^+-ion insertion/extraction reactions [38]. Also, the cyclability of the nanostructured electrodes significantly improved due to the sufficient free spaces to relax the large volume changes during the continuous charge–discharge process

[29]. Hence, various types of nanostructures have been employed as anode materials for LIBs. In order to mitigate the large-volume variation problem of transition metal oxides and to increase the electronic conductivity, carbon coatings have been extensively explored [39–50]. However, the compact carbon coatings on nanoparticles cannot allow residual buffer space to accommodate the large volume change of Fe_3O_4 nanoparticles during Li^+ insertion/extraction. Thus, it remains necessary to exploit an approach for the fabrication of suitable carbon matrix to accommodate volume expansion upon Li^+-ion insertion as well as to increase the electronic conductivity [51–53]. One-dimensional (1D) structure can efficiently improve the performance of Fe_2O_3 as anode material in LIBs due to its excellent electron transport along the lengthways direction and large surface–volume ratio [54–58]. Electrospinning is now a convenient, inexpensive, simple, and versatile method to manufacture the 1D structure including polymer, metal oxide, and organic–inorganic composites [59–62], especially the robust electrode for LIBs. The material obtained by electrospinning can take full advantage of 1D architectures as well as the material can form metal oxide nanoparticles/carbon nanofibers (CNFs) after being calcined under an inert atmosphere. Uniformly dispersing the nano-sized metal oxide into CNFs matrix can significantly enhance the electronic conductivity, buffer the large volume change and pulverization of the electrode, and prevent the agglomerates of nanoparticles [63–71]. The electrospinning technique facilitates to develop 1D metal oxide nano-/microstructure with various morphologies including porous nanowires, nanotubes, nanorods, and tube-in-tube by using non-coaxial electrospinning. This chapter is presenting a detailed overview on the facile fabrication and electrochemical performance of hierarchal Fe_2O_3/Fe_3O_4 nanostructured anode for LIBs.

10.2 Principle of Lithium Ion Batteries

The global lithium-ion battery market is forecasted to grow from USD 36.20 billion in 2018 to USD 109.72 billion by 2026, at a compound annual growth rate (CAGR) of 13.4%, during the forecast period. In recent years, lithium-ion batteries are increasingly being used as the power source for hybrid (HEV) and full-battery electric vehicle (BEV). Over the past couple of years, maximum sales of electric vehicles have accounted by China, the USA, and the European region, which are primarily high-end electric vehicles. Roughly, 1.6 million electric cars were on the roads in China in 2018, followed by 810,000 in the USA. By March 2018, BEV production and sales in China reached 27,673 and 24,127 units, rising 88.35 and 69.21% year-on-year; such figures for plug-in hybrid electric vehicle (PHEV) were 11,210 and 11,171 units, rising 291.21 and 201.47% year-on-year [72]. The industry produced about 660 million units of cylindrical lithium-ion cells in 2012; the 18650 size is by far the most popular for cylindrical cells. The Tesla's Model S electric cars SUVs under 40,000 USD with 85 kWh battery uses 7,104 of lithium ion cells. A 2014 study projected that the Model S alone would use almost 40 percent of estimated global

cylindrical battery production during 2014. Production of the cell was gradually shifted to higher-capacity 3000+ mAh cells.

Based on the use type, LIBs are categorized as primary LIBs and secondary or rechargeable LIBs. A primary battery is one-direction galvanic device designed to be used once and discarded when it is fully discharged, and not recharged with electricity and reused like a secondary or rechargeable battery; i.e., the electrochemical reaction occurring in the cell is not reversible, or it has only discharging process. Lithium primary battery has metallic lithium as anode. Hence, these types of batteries are also referred to as lithium-metal batteries. Presently represent the primary EES systems, with a production higher than 100 million cells/month and about 1500 tons/month of electrode materials. Lithium–manganese dioxide, lithium iron disulfide, lithium thionyl chloride, and lithium iodine batteries are the common lithium primary batteries. Among different lithium primary batteries, lithium thionyl chloride battery has the highest energy density of all lithium-type cells and has a service life of 15–20 years, while lithium iodine batteries provide excellent safety and long service life. In batteries, during discharging, reduction happens on the cathode gaining electrons and oxidation happens on the anode, which is losing electrons, as per the electrochemical reaction shown below [73].

$$\begin{aligned}
&\text{Cathode: } MS_2 + Li^+ + e^- \xrightarrow{\text{discharge}} LiMS_2\\
&\text{Anode: } \quad Li \xrightarrow{\text{discharge}} Li^+ + e^-\\
&\text{Full cell: } Li + MS_2 \xrightarrow{\text{discharge}} LiMS_2\\
&\qquad\qquad\qquad\qquad\qquad\quad (M = \text{Ti or Mo})
\end{aligned}$$

In contrast to lithium primary batteries, lithium secondary batteries, referred as lithium-ion batteries, are rechargeable batteries in which lithium ions move from the negative electrode to the positive electrode during discharge and opposite action happens during charging. Research on LIBs started in the early 1980s, and the principle of the current LIB was completed in 1985 and then first commercialized in 1991 by Sony. Most of the technological developments to date have been directed toward the needs of portable electronics, but now the focus tends to be on the performance demands of medium- and large-scale applications. As shown in Fig. 10.1, typically, LIB consists of three layers: (i) cathode or positive electrode which commonly consists of $LiCoO_2$ [74, 75], $LiNiO_2$ [76], $LiMn_2O_4$ [77], etc., (ii) anode or negative electrode consists of graphitic carbon [78], TiO_2 [79], Fe_2O_3/Fe_3O_4 [80], etc., and (iii) a separating cum electrolyte called gel polymer electrolytes (GPEs) which is permeable to the ions and the electrolyte (e.g., $LiPF_6$ in an organic solvent). GPEs are prepared by immobilization of organic liquid electrolytes, e.g., a 1M solution of $LiPF_6$, $LiClO_4$, or LiTFSI into polymer structures [81–83]. Polymers such as polyethylene oxide (PEO) [84, 85], polyacrylonitrile (PAN) [86, 87], polyvinylidene difluoride (PVdF) [88, 89] and its copolymer polyvinylidene difluoride-*co*-hexafluoropropylene (PVdF-*co*-HFP) [90, 91], and polymethyl methacrylate (PMMA) [92, 93] are among the well-studied materials. As the name implies, the working of a lithium-ion battery mainly relies on repeated transfer of

lithium ions between the anode and the cathode. The electrochemical properties of the electrodes are strongly influenced by the physical and chemical properties of the electrode active material, such as particle size, homogeneity, morphology, and surface area. Lithium-ion polymer batteries (LiPo batteries) are by far the most common commercialized secondary cell polymer battery, with leading technology among other types of metal-ion polymer batteries. A LiPo battery is a rechargeable battery of lithium-ion technology using a polymer electrolyte instead of a liquid electrolyte. LIBs are able to supply continuous energy due to the spontaneous oxidation–reduction reactions occurring at the electrodes. During the charging process (delithiation), Li^+ ions are extracted from the cathodic material by supplying energy by an external source. The extracted Li + ions diffuse in the electrolyte and enter the anodic material (according to the reaction $C_x + LiMO_2 \rightarrow Li_{(1-y)}MO_2 + C_xLi_y$, in the case of a traditional LIB [94, 95]), while electrons are simultaneously the electrons transferred to the positive electrode through the external circuit. In the discharge process (lithiation), the opposite process takes place (i.e., $Li_{(1-y)}MO_2 + C_xLi_y \rightarrow C_x + LiMO_2$, in the considered example): i.e., Li^+-ions, extracted from the anodic material, are re-inserted into the cathodic material, and the cell provides energy. The oxidation and reduction process occurred at two electrodes in the lithium rechargeable batteries as shown below [96, 97].

$$\text{Cathode: } LiMn_2O_4 \rightarrow Li_{1+x}Mn_2O_4 + xLi^+ + xe^-$$
$$\text{Anode: } xLi^+ + xe^- + C_6 \rightarrow Li_xC_6$$
$$\text{Full Cell: } LiMn_2O_4 + C_6LiC_6 + LiMn_2O_4$$

Each combination of the aforementioned materials and compound will slightly influence cost, voltage, cycle durability, and other characteristics of the LiPo batteries. The secondary lithium-ion batteries, in general, operate 3.7 V and demonstrate a capacity of 150 mAh g^{-1} [98].

10.3 Electrode Materials for Lithium Ion Batteries

LIB primarily contains four essential components, namely the anode, the electrolyte, the separator, and the cathode. Typically, LIBs use an intercalated lithium compound as the positive electrode and graphite as the negative electrode. However in the earliest configuration of LIBs metallic lithium or Li–Al alloys was used as the negative electrode, with a variety of chalcogenides (TiS_2, MoS_2, etc.), [73] as the positive electrode in several prototypes and commercial products. Due to safety concerns, lithium metal as an anode material in rechargeable batteries was ultimately rejected. The unavoidable dendrite growth on the lithium metal surface during the repeated cycling cause lithium plating that leads to internal short circuits.

10.3.1 Positive Electrode (Cathode) for Lithium Ion Batteries

The cathode material requires a stable crystalline structure over wide ranges of composition because during the process of lithiation, the oxidation reaction leads to large compositional changes and therefore to unfavorable phase changes [99]. Also, the cathode performance directly depends not only on the electrode microstructure and morphology, but also on the inherent electrochemical properties of the cathode material due to the fact that Li^+-ion exchange with the electrolyte only happens at the electrode–electrolyte interface [100, 101]. The development of electrochemically stable $LiCoO_2$ as a positive electrode leads to the commercialization of the lithium ion battery by Sony, Japan, paved a path to hunt novel electrode materials which provided a step change in the approach to the development of advanced energy storage based on lithium technology [102, 103]. Combining $LiCoO_2$ with graphitic carbon which provided a host for Li^+-ions at low potential thus successfully removed metallic lithium from the LIBs. The domination of LIBs as the power source in the portable electronic and automobile market leads to the subsequent improvements in the LIBs, which forced the scientific community to focus on developing new cathode materials; thus, LMO, NMC, LFP, etc., were introduced. But recently, the introduction of nanocomposites comprised of Sn (theoretical capacity 992 mAh g^{-1}) or Si (theoretical capacity 4200 mAh g^{-1}) led to major developments in anode materials, which require higher-capacity cathode materials to provide optimum utilization of the storage properties.

In LIBs, cathode materials can store energy through two different electrochemical reaction mechanisms, (i) intercalation and (ii) conversion reaction [100]. Conversion-type cathodes undergo a solid-state redox reaction during lithiation/delithiation process, in which there is a change in the crystalline structure, accompanied by the breaking and recombining chemical bonds, while the intercalation cathode materials act as a host for Li^+-ions, so that the ions can insert in or extracted out from the cathode material reversibly. Metal halides such as FeF_2, CoFe, and NiF_2 are examples of conversion-based cathode materials. Due to the high volume expansion, poor electronic conductivity, and hysteresis issues, development of conversion-based cathode materials has faced a lot of challenges [100].

Intercalation-based cathode materials are mainly divided into three categories: chalcogenides, transition metal oxides, and polyanion compounds. Due to the higher operating voltage and higher specific capacity, most of research on intercalation cathode materials is focused on transition metal oxides [100]. $LiCoO_2$, $LiNiO_2$ (LNO) [104], $LiNi_xMn_yCo_zO_2$ (with $x + y + z = 1$ or NMC) [105, 106] are some of the examples for the transition metal oxide-based cathodes in LIBs. Even though the layered crystal structure of LNO is similar to LCO, LNO delivers 20–30% more reversible capacity than LCO, but due to its inherent electrochemical properties [104].

Over-lithiated oxides (OLOs) are relatively new replacement material for the cathode in high-capacity LIBs due to their very high capacity over 250 mAh g^{-1} at high-voltage charge over 4.5 V along with many other enhanced properties. OLOs

have been developed with a variety of stoichiometric variations of the general composition: Li_2MnO_3-$(1-x)LiMO_2$ [107]. The major limitation of OLOs is their initial irreversibility caused by Li_2O formation [105]. Another class of important cathode materials is spinel oxides with a general formula of AB_2O_4. The most famous cathode in this group is $LiMn_2O_4$ (LMO), which is a low-cost, reliable, non-toxic, and a high electrochemical potential material, and delivers a practical capacity of 100–120 mAh g^{-1} (theoretical specific capacity is 148 mAh g^{-1}); however, its reversible capacity is less than that of LCO or LNO. The spinel structure of LMO creates a 3D framework which promotes the easy movement of Li^+-ions [105, 108] and undergoes less damage during continuous charge–discharge cycles in comparison with the anode materials having layered structure, because the continuous two-way transportation of Li^+-ions in the spinel structure does not make large volume change at room temperature. However, at high-temperature LMO shows poor cycle as well as calendar life [105]. The manganese dissolution, structural fatigue, and microcracks are other issues associated with LMO, which lead to poor cycling stability and capacity fading. Because of its low specific capacity and low practical capacity, LMO is not recommended to be used as a single cathode material. It also suffers severely from the Jahn–Teller effect, which is a geometric distortion of a nonlinear molecular system that reduces its symmetry and energy. Hence, the cathode material in the new generation of commercially produced batteries consists of a complementary blend of spinal LMO and layered NMC [109].

$LiFePO_4$ (LFP) olivines are polyanionic compounds developed by John B. Goodenough, who received Nobel Prize, in 2019, at the University of Texas in 1996, and that have attracted a lot of attentions due to their thermal stability, environmental friendliness, very flat potential during charge–discharge processes, and high-power capabilities [105]. Again even in harsh environments, the release of oxygen from the active cathode material is inhibited due to the strong P–O bond in phosphate and this structurally stable material guarantees their safety [110, 111].

10.3.2 Anode Materials for Lithium Ion Batteries

Traditionally in commercial LIB anode, the negative electrode from which electrons flow out toward the external part of the circuit is constructed from graphite and other carbon materials coated on a thin copper foil current collector. However, they suffer from serious safety problems, which have hampered their further development [98, 112]. To replace conventional carbon-based anodes, several studies have focused on exploiting novel anode materials. As a result of extensive research, the anode in LIBs can be fabricated from three distinguished groups of materials having very different electrochemical energy storage mechanisms broadly categorized as (i) intercalation-based materials, (ii) conversion-reaction-based materials, and (iii) alloying-reaction-based materials. The properties of most common anode materials used for lithium-ion batteries are summarized in Table 10.1.

10.3.2.1 Intercalation-Based Materials as Anodes in Lithium Ion Batteries

Graphite in its natural or artificial form is the best representative material in the intercalation-based anode materials first introduced by Rachid Yazami, a Moroccan scientist and engineer in 1980. He established the reversible intercalation of lithium into graphite in an electrochemical cell using a polymer electrolyte. Eventually, his discovery led to the lithium–graphite anode now used in commercial lithium-ion batteries, over US$20B value market. In the intercalation-based anode materials, the lithium ions are electrochemically intercalated into the space between the layers of the active materials. Lithium-ion intercalation in graphite can be described by the

Table 10.1 Summarization of most common anode materials used for lithium-ion batteries

Anode material	Theoretical capacity (mAh g^{-1})	Energy storage mechanism	Properties	
			Advantages	Disadvantages
Graphite	372	Intercalation	High electronic conductivity Nice hierarchical structure Abundant and low-cost resources	Low specific capacity Low rate capacity Safety issues
Nanostructured carbonaceous materials (e.g., carbon nanotube/graphene/carbon nanofibers/porous carbons)	Up to 1750	Intercalation		
Metal oxides (Cu_2O, Fe_3O_4, Co_3O_4, MoO_3, etc.)	375–1170	Conversion reaction	High specific capacity Nice stability	Low Coulombic efficiency Large potential hysteresis
Metal nitrides (M_xN_y, M: Fe, CO, Ni, Cu, Cr, V, Ti, etc.)	400–1300	Conversion reaction		
Metal sulfides (M_xS_y) (Ni_3S_2, FeS_2, MoS_2, SnS, SnS_2, etc.)	447–1230	Conversion reaction		
Metal phosphides $Li_xM_yP_4$ (M: V, Ti, Cu, Fe, Mn) (CoP_3, NiP_3, MnP_4, etc.)	700–1800	Conversion reaction		

(continued)

Table 10.1 (continued)

Anode material	Theoretical capacity (mAh g^{-1})	Energy storage mechanism	Properties	
			Advantages	Disadvantages
Si	4200	Alloying/de-alloying	Highest specific capacity Rich, low-cost, clean resources	Low electronic conductivity Large volume change (100%)
Germanium	1384	Alloying/de-alloying	High specific capacity Good security	Low electronic conductivity Large volume change (100%)
Tin	960	Alloying/de-alloying	Highest specific capacity Rich, low-cost, clean resources High specific capacity Good security	
Phosphorus	2596	Alloying/de-alloying		
Antimony	660	Alloying/de-alloying		
Indium	1012	Alloying/de-alloying		

equation

$$x\mathrm{Li}^{+} + \mathrm{C}_6(\text{in graphite}) + x\mathrm{e}^{-} \longleftrightarrow \mathrm{Li}_x\mathrm{C}_6$$

The reversible lithiation/delithiation (intercalation/deintercalation) reaction proceeds less than 0.25 V versus Li/Li^+, with a practical reversible capacity greater than 360 mAh g^{-1} (theoretically at 372 mAh g^{-1} or 975 mAh cm^{-3}) with high Coulombic efficiency approaching 100% [113, 114]. However, one of the drawbacks with graphitic anode is that some irreversible reactions happen during the first charge (lithiation) process causing a cathodic decomposition of some constituents of the electrolyte. Another major downside of graphite anodes is their low specific capacity, which is addressed in great extent by increasing the surface area of the carbonaceous materials; therefore, the active material can provide more space for the intercalation of Li^+-ions between the graphitic layers leading to the higher specific capacity. Different carbon allotropes such as carbon nanotubes (CNTs), buckminsterfullerene (buck balls), and graphene nanosheets (GNSs) [115] or carbon nanofibers (CNFs) [116] are vastly studied as an alternative to graphite due to their larger surface area as well as higher electronic conductivity which makes them suitable for high rate charging/discharging [117]. Single-wall CNTs are expected to exhibit reversible

capacities somewhere around 300–600 mAh g^{-1} [118], and for graphene the theoretical capacity is about 744 mAh g^{-1}. A reversible specific capacity is as high as 1264 mAh g^{-1} at a current density of 100 mA g^{-1}, and a capacity retention of 718 mAh g^{-1} is reported even at a high current density of 500 mA g^{-1} [115, 116, 119].

10.3.2.2 Conversion Reaction-Based Materials as Anodes in Lithium Ion Batteries

The simple conversion electrochemistry of transition metal oxides (TMOs), sulfides, phosphides, and similar compounds of p-block metalloids shares some interesting and useful electrochemical features with other anode materials [120]. It was already well understood, and different types of anode electrochemistries that qualify the required norms set for the battery application, namely the operating potential of <2 versus Li/Li^+, are categorized as intercalation, alloying, and conversion types. The conversion reaction-based materials are based on the Faradaic reaction represented as follows.

$$M_a X_b + (b \cdot n)Li^+ + ae^- \longleftrightarrow aM + bLi_n X$$

where M is the transition metal such as Ti, V, Cr, Mn, Fe, Co, Ni, Cu, Mo, W, and Ru, X is the anion such as O, N, F, S, and P, and n is the number of negative charges of X [121]. A variety of anode materials are possible in this group by a simple combination of candidates of M and X even without considering multiple oxidation states of M. The theoretical capacity of the conversion-reaction-based anode materials ranges from 350 mAh g^{-1} for Cu_2S to 1800 mAh g^{-1} for MnP_4 [121]. The relatively high theoretical capacity of conversion reaction-based compounds as compared to graphite (372 mAh g^{-1}) makes these materials as ideal anode materials. However, compared to graphitic carbon, these materials have some major down steps including lower Coulombic efficiency, electronic conductivity, inferior cycling stability, and rate capability, which must be dealt with before being used as anode material. In addition, the conversion-reaction-based anode materials undergo large volume changes during lithiation and the following delithiation, which could lead to pulverization or electric isolation leads to the fast capacity fade under cycling. This means that the conversion reactions in conversion-reaction-based anodes would have intrinsically limited reversibility [122, 123]. Again the reaction potentials of conversion-reaction-based anode materials (E_{conv}), at which the potential profiles reach a plateau, are relatively higher than that of graphite. Higher E_{conv} leads to lower cell potential which results in a lower energy density than expected only from capacities [121]. Although intercalation and alloying materials have received the preferred focus by the battery technologist, conversion materials have thus far been left out for any type of practical industrial applications owing to the aforementioned specific shortcomings [124].

10.3.2.3 Alloying Reaction-Based Materials

The third category of anode materials after intercalation and conversion reaction-based materials is the alloying reaction-based materials. This group consists of metals that can be alloyed with lithium such as silicon (Si), germanium (Ge), tin (Sn), and their alloys [114, 125]. In this category, the Li ions are inserted into the structure of anode material during the charge cycle, making an alloy with the anode. The reversible alloying reaction is shown in Eq. 4, where M is the anode material [125].

$$M + xLi^+ + xe^- \longleftrightarrow Li_xM$$

Alloying reaction-based materials are most famous for their high theoretical capacity: 4200 mAh g^{-1} for Si in $Li_{4.4}Si$, 1600 mAh g^{-1} for Ge in $Li_{4.4}Ge$, 993 mAh g^{-1} for Al in LiAl, 992 mAh g^{-1} for Sn in $Li_{4.4}Sn$, and 660 mAh g^{-1} for Sb in Li_3Sb [126]. However, the major disadvantage of these materials is their extremely large volume change during charge and discharge [118]. They experience serious pulverization resulting in electrical isolation of the active materials from electric contact with the conducting agent (carbon black) and the current collector. Among the alloying elements which can be used in this group of anode materials, the vast majority of research and development has been focused on silicon because of its highest capacity and its most serious detrimental volumetric change [126–129].

10.4 Electrospun-Based Iron Oxide Anodes for Lithium Ion Batteries

Iron oxide-based nanocomposites including Fe_3O_4/carbon nanocomposite [43, 49, 130, 131] and Fe_2O_3/carbon nanocomposites [132–134] have been fabricated and studied extensively as electrode materials for lithium-ion batteries. Iron oxide is a paramagnetic material which has only two unpaired electrons. Because the lower number of unpaired electrons irons oxide is less magnetic than iron, which has four unpaired electrons. Iron (III) oxide or ferric oxide is the inorganic compound with the formula Fe_2O_3. It is one of the three main oxides of iron, the other two being iron (II) oxide (FeO), which is rare, and iron (II,III) oxide (Fe_3O_4), which also occurs naturally as the mineral magnetite. Fe_2O_3 can be obtained in various polymorphs. In the main ones, α and γ, iron adopts octahedral coordination geometry; i.e., each Fe center is bound to six oxygen ligands. α-Fe_2O_3 has the rhombohedral, corundum (α-Al_2O_3) structure and is the most common form, which occurs naturally as the mineral hematite while γ-Fe_2O_3 has a cubic structure and occurs naturally as the mineral maghemite. γ-Fe_2O_3 is metastable and converted from the alpha phase at high temperatures. γ-Fe_2O_3 is ferromagnetic, and however ultrafine particles smaller than 10 nm are superparamagnetic. α-Fe_2O_3, γ-Fe_2O_3, and Fe_3O_4 are explored as electrode materials in LIBs. The crystal structure of Fe_2O_3 is displayed in Fig. 10.2

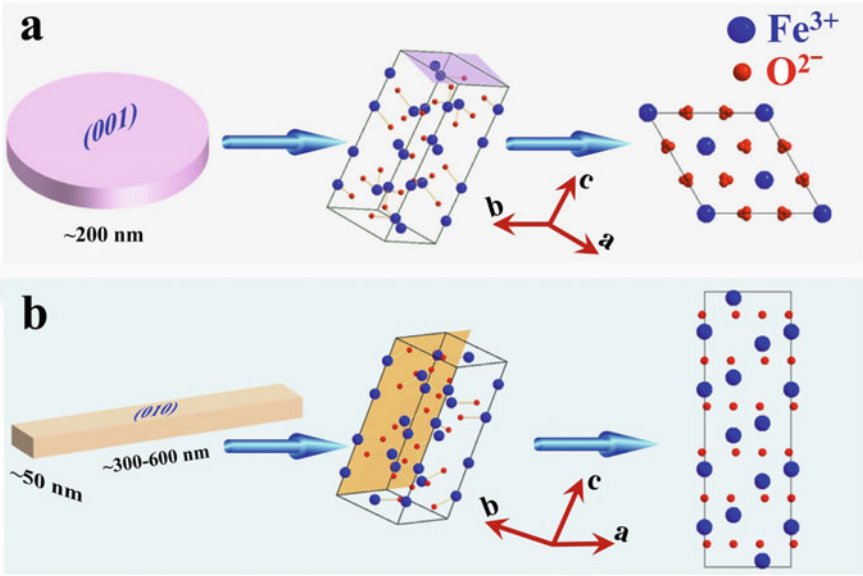

Fig. 10.2 The surface atomic configurations in **a** the (001) plane and schematic hematite structure project along {001} and **b** the (010) plane and schematic hematite structure projected along {010}. Adapted and reproduced from Ref. [162]. Copyright 2016 Springer

[162]. In principle, lithium storage capacity of iron oxides is mainly delivered through the reversible conversion reaction between lithium ions and metal oxide forming metal nanocrystals dispersed in a Li_2O matrix. Even though this material is abundant, inexpensive, and environmentally friendly and has high theoretical capacity (Fe_3O_4: 924 mAh g^{-1} [135]; Fe_2O_3: 1005 mAh g^{-1} [136]), they are fraught with several problems such as poor electronic conductivity, higher volume expansion, and poor cycling stability. Among the major disadvantages, the cycle deterioration is the most important one which is caused by several factors such as the decomposition of the electrolyte solution and loss of the conductive path owing to electrode collapse [137]. In addition, large volume change of the anode material during the continuous charge–discharge cycling causes the cracking of the electrode, loose the contact with current collector, and destruction of the solid electrolyte interface (SEI), which result in the breaking of the continuous conductive path. Reducing the extent of volume expansion and contraction would suppress these problems in a great extent. Nanoscale processing of active material particles has been studied for this purpose [138–140]. Carbon coating [141], mixing with electronically conducting materials such as conducting carbon [142], carbon nanotubes [143], and graphene [144], is the commonly adopted technique to control the extent of volume change and for improving the electronic conductivity of iron oxides. Although the volume change ratio depends on material-specific quantities, it is possible to control the extent of volume change by controlling the particle size of the active material. Owing to the

formation of short Li^+-ion diffusion length by the size reduction of the active material to nanoscale, the chemical reaction resistance also get reduced. However, there are various processing difficulties associated in the use of nano-sized active material particles and nanoscale processing such as poor dispersibility due to an increase in the van der Waals force, low initial Coulombic efficiency due to high specific surface area, and low safety due to high chemical activity. To solve out these issues, electrodes prepared using composites of nanoscale active materials and carbon materials have been reported extensively [140], owing to the reduction in interfacial area between the electrolyte and active material by the composite effect, which suppresses the SEI growth, thereby improving the Coulombic efficiency.

Carbon coating on iron oxide nanoparticles can form 0D nanospheres [145, 146] 1D nanowires [36, 147], 2D nanoflakes [148, 149], and 3D structures of porous carbon foam loading iron oxide [43, 45]. Different methods such as solid-state reaction [150], hydrothermal process [151], solgel method [152], spray-drying technique [153], vacuum sintering [154], and vacuum decomposition are some of the commonly used methods for doing the carbon coating. Electrospinning is one of the unique carbon coating methods and has been used to fabricate 1D hybrid carbon coating iron oxide nanofibrous composites [79, 155–158], 1D iron oxide nanofibers [12, 159], and 1D carbon nanofibers for Li-ion batteries [160, 161]. The method can embed the iron oxides into a conductive carbon by subsequent heat treatment which enhances the electrochemical properties effectively due to the increased electronic conductivity. The uniformly coated nanometer-thick carbon layer on the active material (iron oxide) acts as the mechanical buffer, which prevents or minimizes the large volume expansion and cracking of electrode during the continuous charge–discharge cycles.

10.4.1 Electrospun Fe_2O_3/Fe_3O_4 Nanostructures

Different coating methods for the preparation of nanostructures such as chemical vapor deposition (CVD) [163], atomic layer deposition (ALD) [164, 165], electrochemical deposition (ECD) [166], and chemical bath deposition (CBD) [167–169] or the conventional synthetic strategies such as hydrothermal method [170] and scaffold-assisted synthesis method [170] are reported for the fabrication of nanostructures of Fe_2O_3/Fe_3O_4. Unfortunately, these methods need to involve the multistep growth of designed shell materials on various removable or sacrificial templates, which suffers from severe drawbacks. These methods are time consuming; tedious, high-temperature, and complicated processes need expensive equipment. Compared to the other synthesis methods, electrospinning is a facile, cost-effective, and flexible platform for one-dimensional (1D) robust Fe_2O_3/Fe_3O_4 nanostructures. This versatile method offers several advantages, such as high yield, mass production, easy control over the morphology, and high degree of reproducibility of the obtained materials [171–177]. More importantly, the electrospun nanofibers possess high surface-to-volume ratios due to the formation of super long scale in length of thin fibers, the completely interconnected pore structure, the porous substructure formed on

the fiber during annealing, nano- to submicron size fiber diameters, and the great control over the morphology by simply changing the electrospinning process, solution, or ambient parameters [172]. When used these electrospun Fe_2O_3/Fe_3O_4 nanostructured materials as electrode in lithium-ion batteries, the large specific surface area and sufficient void spaces not only tolerate the volume change during the Li^+-ion intercalation, but also endow with more open channels for ions and electrons to migrate rapidly, resulting in the improved electrochemical performances. There are significant number of studies reported on the preparation of F_2O_3-/Fe_3O_4-based nanostructured anodes having different morphologies such as nanotubes [159, 178], nanorods [162, 179–182], porous structure [158, 183], microbelt [9], or hollow fibers [12, 184].

10.4.1.1 Porous Fe_2O_3/Hollow Fe_3O_4 Nanotube

A nanotube is a nanoscale material that has a seamless tubelike structure. Among the various nanostructures of Fe_2O_3 such as nanoparticles [185], nanorods [26, 186] and nano fibers [187, 188] etc., (1D) Fe_2O_3/Fe_3O_4 nanotubes [159, 170, 189] gained munch attraction due to their advantages properties, including the increase contact surface area between electrolyte and active materials, shorten migration path for Li+ and electron, and accommodate the volume variations via additional void space during cycling.

Sun et al. [170] prepared 1D porous Fe_2O_3 nanotubes with 2-μm length, 220-nm outer diameter, and 65-nm wall thickness via a low-temperature hydrothermal method followed by thermal treatment. The resulted porous Fe_2O_3 nanotubes exhibited enhanced electrochemical properties in terms of lithium storage capacity (1050 mAh g^{-1} at 100 mA g^{-1} rate), initial Coulombic efficiency (78.4%), cycle performances (90.6% capacity retention at 50th cycle), and rate capability (613.7 mAh g^{-1} at 1000 mA g^{-1} rate). 1D porous Fe2O3 nanostructures have also been synthesized via a SiO2 scaffold method, exhibiting the initial discharge and charge capacities of 1304.3 and 950.9 mAh g^{-1} at a current density of 100 mA g^{-1}, respectively [170]. Also, the porous Fe_2O_3 nanorods deliver a capacity of 671 and 541 mAh g^{-1} at current densities of 1000 and 2000 mA g^{-1}, respectively, showing good rate capability. Although the aforementioned porous Fe2O3 nanotubes showed the enhancement of lithium storage capacities, to fabricate porous Fe2O3 nanotubes with satisfied properties via a facile technology is still an appealing challenge. Hence, the robust electrospun Fe_2O_3 nanotubes are prepared and studied its electrochemical properties in LIBs.

Porous Fe_2O_3 [159] and Fe_3O_4/C [178] nanotubes were prepared by electrospinning a solution of iron (III) acetylacetonate and PVP (for porous Fe_2O_3 nanotubes) or iron (III) acetylacetonate and polyacrylonitrile (PAN) (10:8 wt./wt.) along with a 40% mineral oil on weight of iron (III) acetylacetonate (for Fe_3O_4/C nanotubes). First, the Fe_2O_3 or Fe_3O_4/C precursor fiber was prepared and then the fibers are heat-treated to transform to the porous hollow nanotubes. Fe_2O_3 precursor nanofibers (Fig. 10.3a, b) having an average fiber diameter of 520 nm possess continuous fibrous geometry

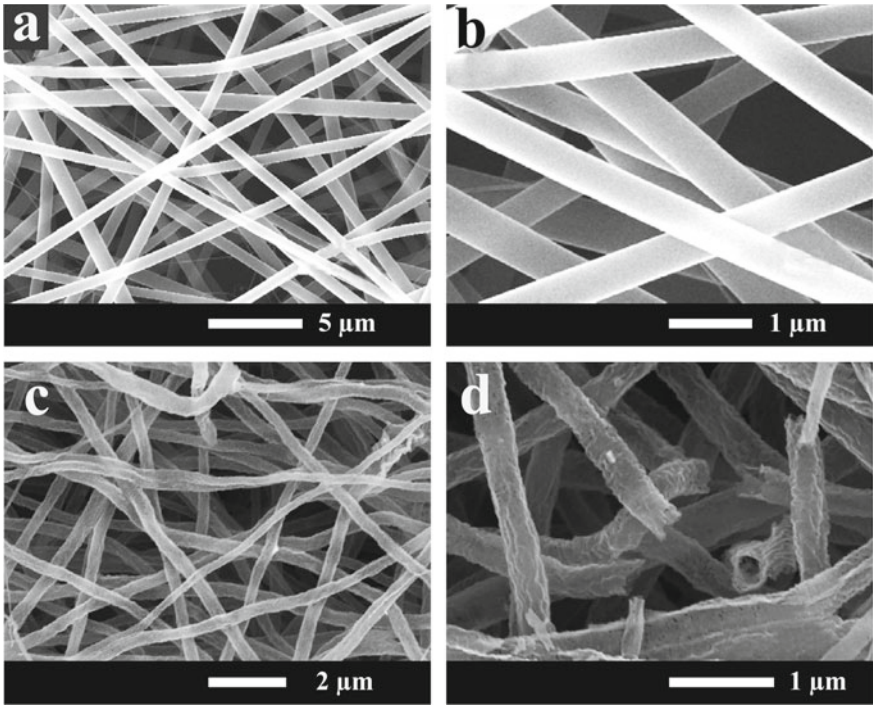

Fig. 10.3 **a**, **b** Low- and high-resolution images of precursor fibers, **c**, **d** FE-SEM images of porous Fe_2O_3 nanotubes. Adapted and reproduced from Ref. [159]. Copyright 2015 Elsevier

with a relatively smooth surface and without any pores or hierarchical nanostructure were first prepared by electrospinning and then annealed at 500 °C. After annealing, the as-prepared sample inherits the continuous 1D nanostructures from the precursor fibers and shows a large quantity of tubelike structures having average diameter of 400 nm (Fig. 10.3c, d); i.e., the diameter of the precursor fiber gets reduced by the shrinkage at higher temperature. For the production of Fe_3O_4/C nanotubes, the as-spun nanofibers were pre-oxidized in air at 250 °C for 2 h to follow by the carbonization at 600 °C for 2 h under high-purity argon atmosphere. The resultant nanotubes have outer diameter range from 200 to 400 nm and length of several millimeters.

During the electrospinning process, when the fibers are spun out from the spinning needle, the solvent will evaporate rapidly from the surface of fibers. This leads to the formation of a concentration gradient of solvent along the radial direction of the fibers, as illustrated in Fig. 10.4a; hence, the concentration at the center of the fibers is usually high than that of the surface. Due to the rapid evaporation of the solvent, the PAN will solidify on the surface of fiber. During the solidification process, the AAI and PAN will be extracted and reside at the shell of the fiber due to the rapid phase separation result from their poor solubility in mineral oil. Hence, the rapid evaporation of solvent produces a region near the fiber surface enriched in

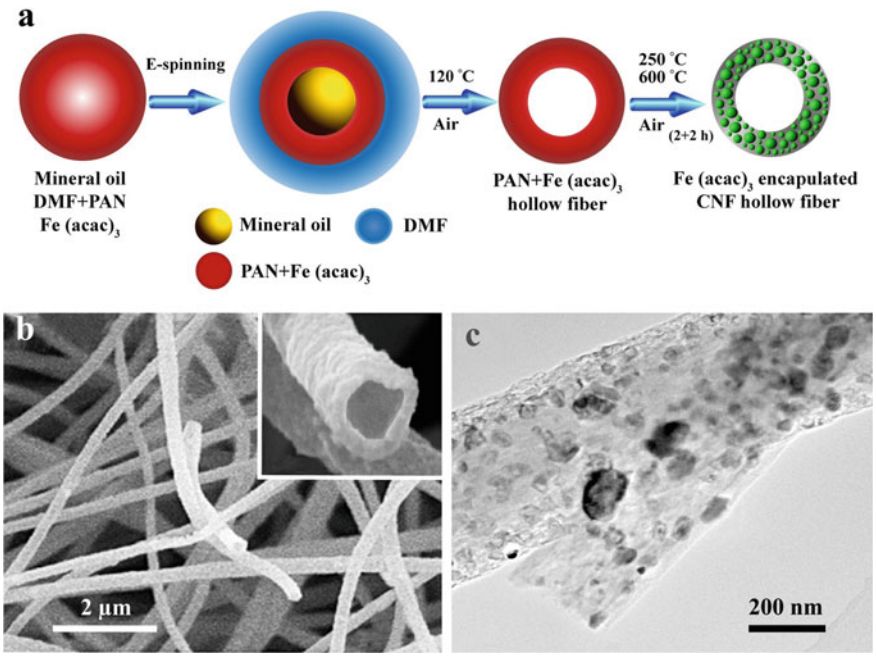

Fig. 10.4 **a** Schematic illustration of one step method to fabricate 1D Fe_3O_4/C nanotubes by electrospinning, **b** SEM image on the surface morphology of the final Fe_3O_4/C nanofibers, and the lower-left corner inset is an enlarged view of a single nanotube, and the scale bar is 200 nm, **c** TEM images of the Fe_3O_4/C nanotube. Adapted and reproduced from Ref. [178]. Copyright 2014 Elsevier

PAN/AAI, and the mineral oil would diffuse from the surface to the core of the fiber. With the continuing evaporation of the solvent, the concentration of PAN/AAI decreases continuously from the surface to the center of fiber, and the mineral oil tends to congregate at the center of fibers, as displayed in Fig. 10.4a. Further, the mineral oil at the center of fiber might evaporate through the wall of the nanotubes and PAN/AAI nanotubes were collected on the target. During the carbonization at 600 °C in Ar atmosphere, PAN would be decomposed and carbonized completely leading to the formation of Fe_3O_4/C nanotubes obtained. The tubes have a wall thickness of 40 and 150 nm hollow cores as shown in Fig. 10.4b, and it shows a roughness surface that can be distinctly observed from Fig. 10.4c.

On contrary, during the production of porous Fe_2O_3, the electrospun precursor nanofibers showed a smooth surface without porous or hollow structures. When the precursor fiber is sintering in air atmosphere, the degradation of the side chain of PVP formed through the intermolecular cross-linking reaction and the decomposition of iron acetylacetonate occur simultaneously. Upon increasing the temperature, both PVP and iron acetylacetonate would be oxidized. The oxidation of PVP results in the volatilization and evolution of CO_2, while the oxidation of iron acetylacetonate resulted in the formation of Fe_2O_3 nanoparticles. The outward diffusion of CO_2

generates a pressure to compress the Fe_2O_3 nanoparticles on the surface region of the fiber and forms a porous shell. Then, the porous shell allows CO_2 effusion from the regions below the shell in the fiber and the iron precursor in the inner part of the fibers would move toward the surface which is presumably accelerated by gaseous species that are produced by the oxidation of PVP, and crystallized into Fe_2O_3 nanoparticles. Finally, these Fe_2O_3 nanoparticles get connected together to generate porous Fe_2O_3 nanotubes. However, the formation of porous annotate greatly depends on the concentration iron precursor (iron acetylacetonate) in the electrospunned precursor fiber. To get more insight into the actual evolution process of the Fe_2O_3 nanostructures, we carry out a series of concentration-dependent experiments which samples are prepared by adjusting the concentration of iron acetylacetonate in the electrospun precursor solution. The precursor fiber having iron acetylacetonate higher than about 45% in the precursor electrospun fibers resulted in the formation of Fe_2O_3 nanotubes. If the concentration of iron precursor is less than 45% obviously, it results in the formation of a few Fe_2O_3 nanoparticles, which is difficult to keep the robust frame of the nanotube shell. As a result, the collapse of the tube structure results in the formation of the nanobelts (Fig. 10.5a). When the iron precursor concentration is lower than 37%, only nanobelts are formed (Fig. 10.5b), while the increase in concentration to 47% forms both nanobelts and nanotubes (Fig. 10.5c). When the iron precursor concentration is further extended to about 50%, the increase progressively encourages the formation of a large number of Fe_2O_3 nanoparticles; as a result, the Fe_2O_3 porous nanotubes appear (Fig. 10.5d). Hence, the evolution of Fe_2O_3 nanostructures could be controllably synthesized by adjusting the concentration of the electrospun precursor solution (Fig. 10.5e).

The cyclic voltammetry studies showed three cathodic peaks correspond to the potentials 1.55, 0.89, and 0.55 V, indicating the different lithiation steps [12, 156, 190, 191]. The peaks at 1.55 and 0.89 V correspond to the intercalation of Li + ions into the crystal structure of porous Fe_2O_3 nanotubes and the transformation from hexagonal α-$Li_xFe_2O_3$ to cubic $Li_2Fe_2O_3$ without any crystal structure destruction. The high intensity peak observed at 0.55 V corresponds to the crystal structure destruction accompanied by the complete reduction of iron from Fe(III) to Fe(0) and the decomposition of electrolyte. The anodic polarization peaks observed at 1.85 V correspond to the oxidation of Fe(0) to Fe(II) and Fe(III) to re-form Fe_2O_3. Compared to the first cycles, the subsequent cycles are significantly different, which is due to irreversible phase transformation during lithium insertion and extraction in the initial cycle. During the second cathodic process, the peaks at 1.55 and 0.89 V disappear, which indicates lithium insertion and irreversible phase transformation of hexagonal α-$Li_xFe_2O_3$ to cubic $Li_2Fe_2O_3$. Also, a decrease in the peak intensity with the number of cycles is observed, which indicates that the capacity is decreased during cycling. However, the CV curves starts to overlap after the third cycle cathodic scan, which indicate the reversibility and capacity stability the continuous charge-discharge processes. The galvanostatic charge–discharge profiles of the porous Fe_2O_3 are consistent with CV curves [159].

The porous Fe_2O_3/Li metal half cells assembled by using Celgard 2400 membrane as the separator and 1M $LiPF_6$ in ethylene carbonate/dimethyl carbonate

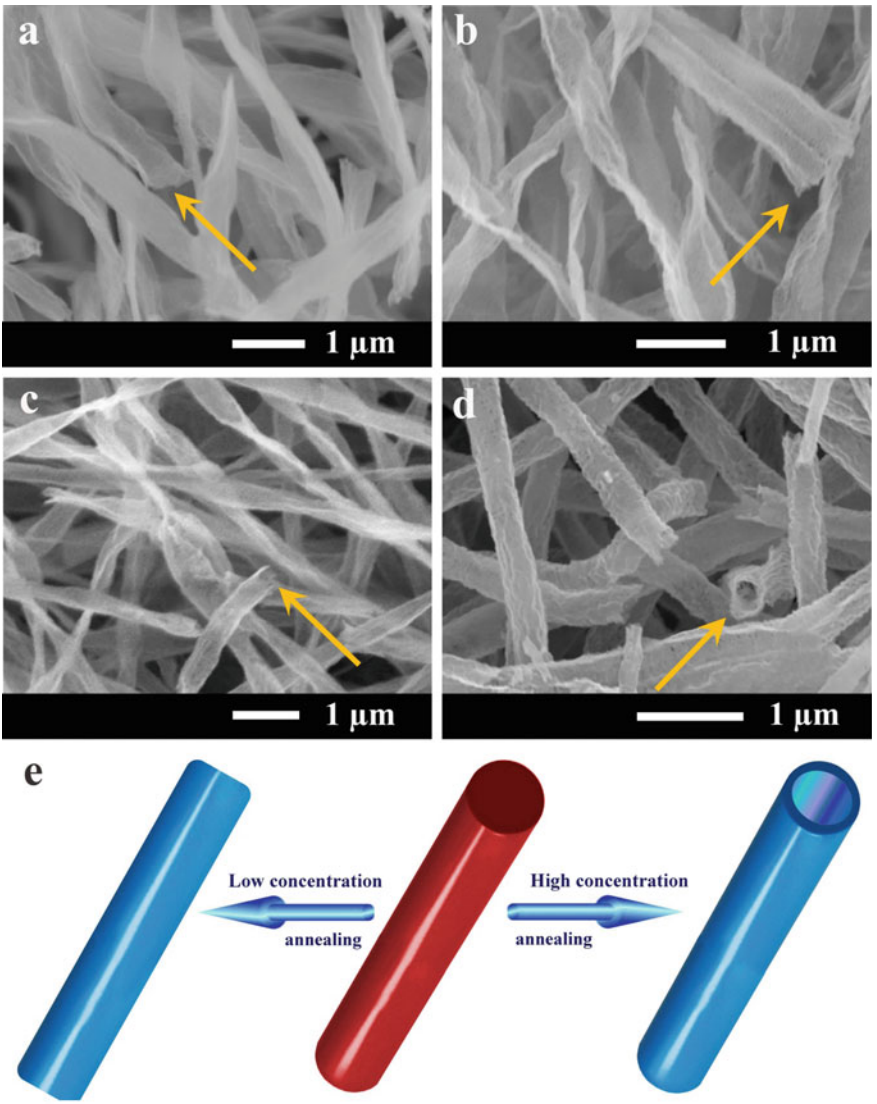

Fig. 10.5 SEM images on the surface morphology of Fe_2O_3 nanostructures obtained by adjusting the quantity of iron acetylacetonate (g): **a** 0.2, **b** 0.3 **c** 0.4, and **d** 0.5, respectively in the electrospun precursor solution. **e** Possible formation mechanism of Fe_2O_3 nanostructures. Adapted and reproduced from Ref. [159]. Copyright 2015 Elsevier

(EC/DMC,1:1 v/v) as the electrolyte delivered an initial charge and discharge capacities of around 1045 mAh g^{-1}, at a current density of 100 mA g^{-1}. Particularly, the porous Fe_2O_3 nanotubes still exhibit an excellent cyclic performance at a much higher current density of 200 mA g^{-1}, and the capacity reaches 988 mAh g^{-1} after 250 discharge and charge cycles. The Coulombic efficiency rises rapidly in the subsequent cycles, reaching up to 95% at the 5th cycle, and remains above 98% after 50 cycles, suggesting an excellent reversible Li^+-ion intercalation/extraction performance. The specific reversible charge and discharge capacity decrease slightly up to the initial 50 cycles and reach 513 and 524 mAh g^{-1}, respectively, and then increase significantly and reach over 995 and 988 mAh g^{-1} by 250th cycle. The porous Fe_2O_3 also showed good rate capability [159]. Similarly, the Fe_3O_4/C nanotubes also showed good charge–discharge cycling stability and rate capability. In the half cell studies using M $LiPF_6$ in ethylene carbonate, diethyl carbonate and ethyl methyl carbonate (EC/DMC/EMC, 1:1:1 vol) as the electrolyte and Celgard 2400 polypropylene as separator showed an initial discharge and charge capacity of 1102 and 727 mAh g^{-1}, with a Coulombic efficiency of only 66% at a current density of 0.15 °C. The significantly higher capacity loss (34% loss) during the first cycle [178] is corresponding to the formation of SEI layer and the incomplete conversion reaction [192, 193]. When the cell is cycled at 1600 mA g^{-1}, the cell delivers a very stable capacity of 350 mAh g^{-1}, and when the current density is switched back to 0.15 °C, a capacity about 600 mAh g^{-1} is delivered, which is about 100 mAh g^{-1} less compared to the first cycles at 0.15 °C [178].

In both porous Fe_2O_3 and Fe_3O_4/C electrodes, an initial capacity loss (25–35%) is observed. Similar irreversible capacity loss was noted with other metal oxides or metal oxide combinations reported in previous literature [12, 193, 194].

Compared to Fe_3O_4/C nanofibers prepared by a controlled fabrication process, sample fabricated according to Wang's reports [157] good electrochemical performance. The charge–discharge studies at a current density of 0.15 °C displayed a quick drop-down in discharge capacity to 300 mAh g^{-1} after 100 cycles, which is about 50% discharge capacity of the F_3O_4/C. More clearly, F_3O_4/C nanotube shows negligible capacity decreases from the 2nd cycle onward and displayed a discharge capacity as high as 600 mAh g^{-1} (85% of the second cycle capacity) after 100 cycles at a current density of 0.15 °C [178]. The lackluster cycling performance of Fe_3O_4/C nanofibers is due to the solid structure of the nanofiber; hence, there is no enough space to accommodate the mechanical stress of Fe_3O_4 nanoparticles along the fiber axis of the nanofibers. The substantially subdued capacity fade in Fe_3O_4/C nanotubes is due to the hollow nanotube structure having larger surface-to-volume ratio than that of 1D nanofibers, which could effectively accommodate large volume changes associated with Li^+-ions insertion/extraction. In addition, the tubular structure can increase the surface area accessible to the electrolyte facilitating the diffusion of Li^+ ions at the interior and exterior of the nanotube. The charge–discharge capacity fade under continuous cycling is mainly due to the pulverization of original aggregation of Fe_2O_3 particles by the huge volume expansion and contraction during the Li^+-ion intercalation/extraction process and resulting in the loss of electrical connectivity between the particles and current collector.

A novel process for the preparation of aggregate-free metal oxide nanopowders with spherical (0D) and non-spherical (1D) hollow nanostructures was introduced. Carbon nanofibers embedded with iron selenide (FeSe) nanopowders with various nanostructures are prepared via the selenization of electrospun nanofibers. Ostwald ripening occurs during the selenization process, resulting in the formation of a FeSe-C composite nanofiber exhibiting a hierarchical structure. These nanofibers transform into aggregate-free hollow Fe_2O_3 powders via the complete oxidation of FeSe and combustion of carbon. Indeed, the zero-dimensional (0D) and one-dimensional (1D) FeSe nanocrystals transform into the hollow-structured Fe_2O_3 nanopowders via a nanoscale Kirkendall diffusion process, thus conserving their overall morphology. The discharge capacities for the 1000th cycle of the hollow-structured Fe_2O_3 nanopowders obtained from the FeSe–C composite nanofibers prepared at selenization temperatures of 500, 800, and 1000 °C at a current density of 1 A g^{-1} are 932, 767, and 544 mAh g^{-1}, respectively; their capacity retentions from the second cycle are 88, 92, and 78%, respectively. The high structural stabilities of these hollow Fe_2O_3 nanopowders during repeated lithium insertion/desertion processes result in superior lithium-ion storage performances.

Figure 10.6 outlines the mechanism of the formation of Fe_2O_3 nanopowders exhibiting hollow nanostructures of different dimensions via the nanoscale Kirkendall diffusion process. Following the selenization processes at different temperatures (i.e., 500, 800, or 1000 °C), the electrospun nanofibers (Fig. 10.6a) were transformed into the hierarchical nanostructures. Selenization of the iron components located close to the nanofiber surface resulted in the formation of FeSe nanocrystals during the early stages of the process. Ostwald ripening then occurred during further selenization to yield the hierarchical FeSe–C composite nanofiber. In this process, the ultrafine FeSe nanocrystals formed inside the carbon nanofiber diffused to the surface to produce FeSe crystals via Ostwald ripening. Complete selenization at 500 °C resulted in the carbon nanofiber being uniformly embedded with ultrafine FeSe nanocrystals (Fig. 10.6b). However, at higher selenization temperatures (Fig. 10.6c), crystal growth occurred via the segregation of nanocrystals and spheroidization due to melting. Finally, the hierarchical FeSe–C nanofibers transformed into hollow aggregate-free Fe_2O_3 nanopowders (Fig. 10.6d, e) via the complete combustion of carbon and oxidation of FeSe. Furthermore, as shown in Fig. 10.7, FeSe nanocrystals with 0D and 1D structures transformed into the hollow-structured Fe_2O_3 nanopowders via a nanoscale Kirkendall diffusion process, thus conserving their overall morphology. For simplicity, the hollow Fe_2O_3 nanopowders obtained from the FeSe-C composite nanofibers prepared at 500, 800, and 1000 °C are referred to as "Sel.500-Oxi.600," "Sel.800-Oxi.600," and "Sel.1000-Oxi.600," respectively [1].

10.4.1.2 α-Fe_2O_3 Nanorods

Nanorods are one of the nanostructured entities, reported as electrodes in LIBs. Different synthesis techniques such as forced hydrolysis, solgel synthesis, template

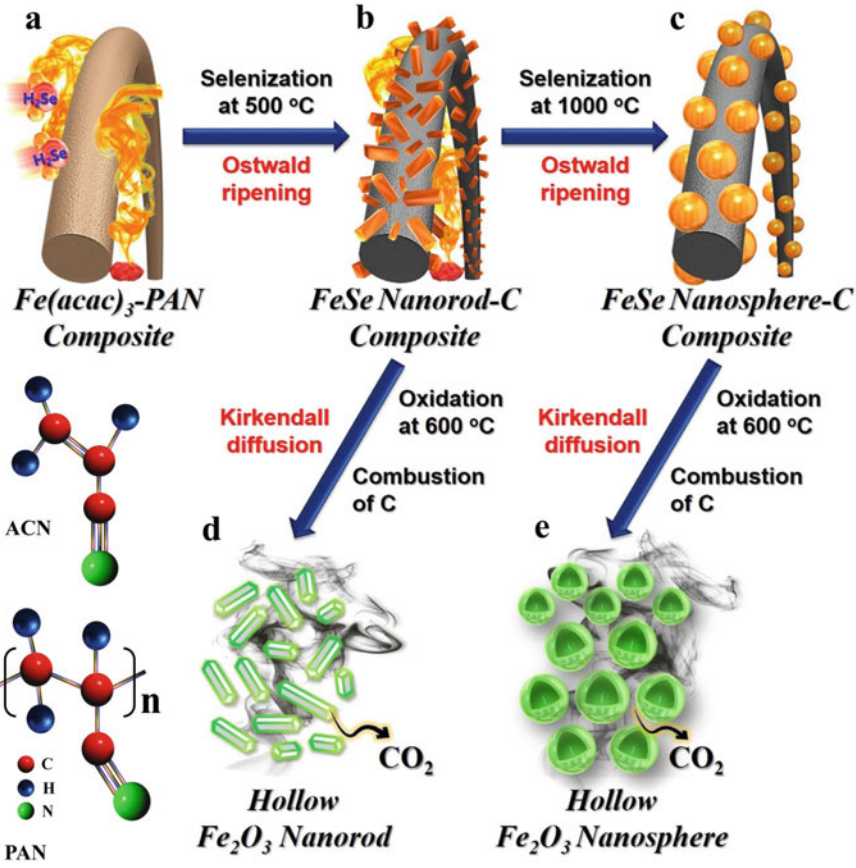

Fig. 10.6 Formation mechanism of the hollow-structured Fe_2O_3 nanopowders with 0D and 1D structure. Adapted and reproduced from Ref. [182]. Copyright 2016 Springer

methods, molten salt process, spray pyrolysis, hot plate method, hydrothermal method, and co-precipitation technique have been adopted to prepare various nanostructures of hematite [34, 134, 191, 195–200]. Nanoscale Kirkendall diffusion and Ostwald ripening processes, in which filled structures are transformed into hollow structures during heat treatment, have been applied recently for the preparation of hollow nanospheres (0D) in the absence of templates [182, 201–205] α-Fe_2O_3 nanorods [156] and bubble-nanorod-structured Fe_2O_3-carbon nanofibers [179] prepared by electrospinning are reported as high performance anode in LIBs.

The α-Fe_2O_3 nanorods are synthesized by electrospinning of polyvinylpyrrolidone (PVP)/ferric acetylacetonate ($Fe(acac)_3$) composite precursors and subsequent annealing at 500 °C for 5 h. The phase separation of $Fe(acac)_3$ and PVP process involving a polymer/precursor forms "islands" that account for the generation of α-Fe_2O_3 nanorods having average diameter of the nanorods is found to be 150 nm

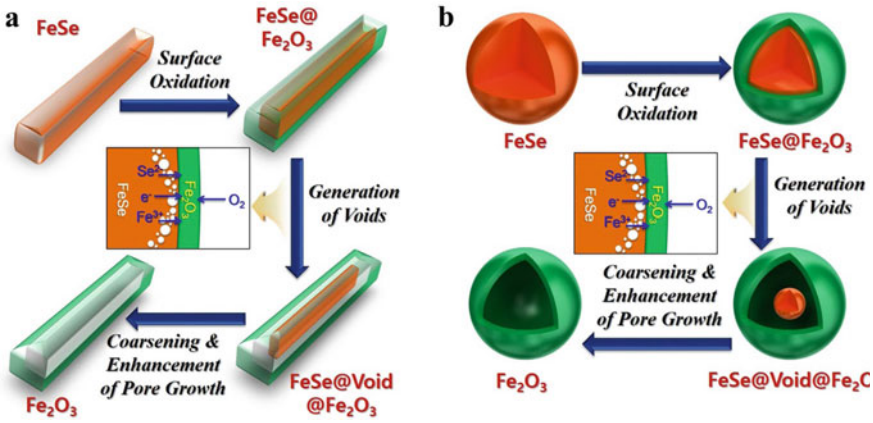

Fig. 10.7 Conversion reaction of the FeSe filled structure into Fe_2O_3 hollow structure by nanoscale Kirkendall diffusion effect, **a** hollow-structured Fe_2O_3 nanopowder with 1D and **b** hollow-structured Fe_2O_3 nanopowder with 0D. Adapted and reproduced from Ref. [182]. Copyright 2016 Springer

upon heat treatment. The annealed electrospun α-Fe_2O_3 nanorods are composed of agglomerates of nano-sized α-Fe_2O_3 particles. The electrospun α-Fe_2O_3 nanorods exhibit a high reversible capacity of 1095 mAh g^{-1} at 0.05 °C, are stable up to 50 cycles (with capacity retention of 93% between 2 and 50 cycles), and also show high rate capability, up to 2.5 °C. At a current rate of 2.5 °C, α-Fe_2O_3 nanorods deliver a discharge capacity of 765 mAh g^{-1} and when the current rate is reduced from 2.5 to 0.1 °C after 70 cycles, still a reversible capacity of 1090 mAh g^{-1} is obtained showing the good rate capability of the material. The high rate capability and excellent cycling stability can be attributed to the unique morphology of the macroporous nanorods comprised of interconnected nano-sized particles [156].

The structure denoted as "bubble-nanorod composite" is synthesized by introducing the Kirkendall effect into the electrospinning method. Bubble-nanorod-structured Fe_2O_3/C composite nanofibers, which are composed of nano-sized hollow Fe_2O_3 spheres uniformly dispersed in an amorphous carbon matrix, are synthesized as the target material using $Fe(acac)_3$-PAN composite solution as the precursor. Post-treatment of the electrospun precursor nanofibers at 500 °C under 10% H_2/Ar mixture gas atmosphere produces amorphous FeO_x/carbon composite nanofibers, and the further post-treatment at 300 °C under air atmosphere produces the bubble-nanorod-structured Fe_2O_3/C composite nanofibers. The solid Fe nanocrystals formed by the reduction of FeO_x are converted into hollow Fe_2O_3 nanospheres during the further heating process by the well-known Kirkendall diffusion process [179].

The formation mechanism of bubble-nanorod-structured Fe_2O_3/C composite nanofibers is schematically displayed in Figs. 10.8 and 10.9. During the carbonization at 500 °C, the PAN gets decomposed to form the carbon matrix and the decomposition of iron acetylacetonate produced FeO_x, which is uniformly dispersed in carbon matrix resulting in the carbon composite nanofibers. The significantly large amount

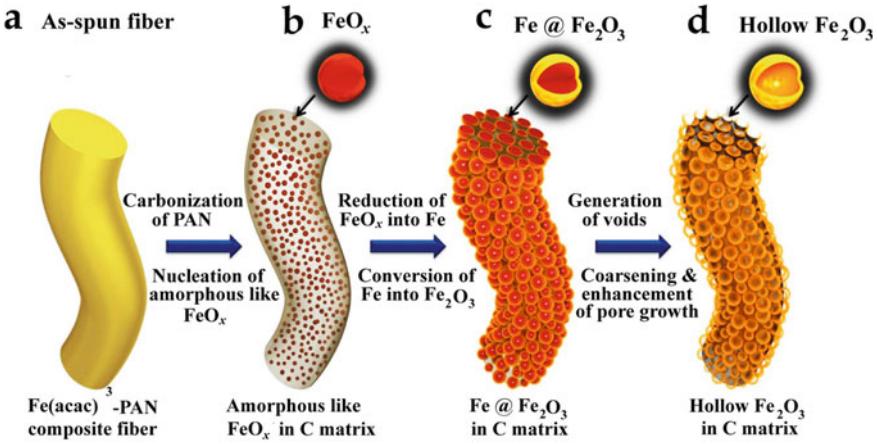

Fig. 10.8 Formation mechanism of bubble-nanorod-structured Fe_2O_3/C composite nanofiber by Kirkendall-type diffusion. Adapted and reproduced from Ref. [179]. Copyright 2015 American Chemical Society

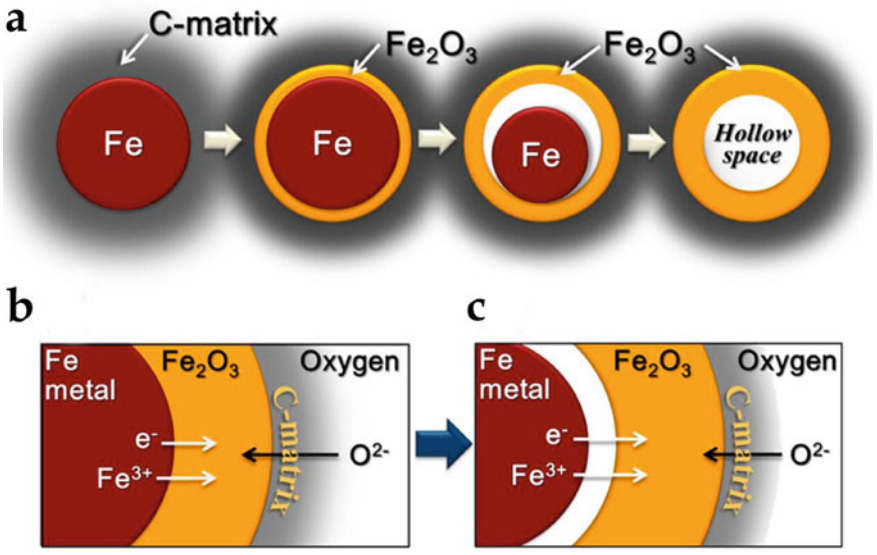

Fig. 10.9 **a** Formation mechanism of hollow Fe_2O_3 nanosphere in the bubble-nanorod-structured Fe_2O_3 carbon composite nanofiber by Kirkendall effect, **b**, **c** its chemical conversion process in the surface region of a sphere. Adapted and reproduced from Ref. [179]. Copyright 2015 American Chemical Society

of carbon in the fiber disturbed the crystal growth of FeO_x. The subsequent post-treatment of the FeO_x/carbon composite nanofibers at 300 °C under air atmosphere produced the bubble-nanorod-structured Fe_2O_3C composite nanofiber. Reduction of FeO_x crystals surrounded by the carbon matrix into Fe metal occurred during the post-treatment under air atmosphere by the following equation:

$$FeO_x(s) + xC(s) \rightarrow Fe(s) + xCO(g)$$

The crystal growth of Fe formed ultrafine Fe nanocrystals uniformly dispersed within the carbon nanofibers during the early stage of post-treatment by the consumption of some amount of carbon. The solid Fe nanocrystals were converted into hollow Fe_2O_3 nanospheres during the subsequent heating process by the well-known Kirkendall effect. The Kirkendall effect, a vacancy flux, and subsequent void formation process resulting from diffusivity differences at inorganic interfaces were first reported by Aldinger [206]. The Kirkendall effect results in the formation of a thin Fe_2O_3 layer on the Fe metal surface (Fig. 10.8c), followed by simultaneous outward diffusion of Fe cations through the oxide layer and inward diffusion of oxygen into the nanospheres, creating an intermediate Fe@Fe_2O_3 core–shell structure (Fig. 10.9b). Fe cations diffused outward more quickly than oxygen diffused inward, which is consistent with the larger ionic radius of oxygen anions (140 pm) than Fe cations (Fe^{2+} is 76 pm, and Fe^{3+} is 65 pm). Accordingly, Kirkendall voids were generated near the Fe/Fe_2O_3 interface during vacancy-assisted exchange of the material via bulk interdiffusion (Fig. 10.9c), which gave rise to coarsening and enhancement of pore growth in the spheres (Fig. 10.8d). Complete conversion of Fe metal into Fe_2O_3 by Kirkendall-type diffusion resulted in the bubble-nanorod-structured Fe_2O_3C composite nanofibers (the highly crystalline structure of the hollow Fe_2O_3 nanofibers). The figure shows the TEM image and elemental mapping of the nanofibers post-treated at 500 °C under H_2/Ar mixed gas atmosphere. The elemental mapping images shown in Fig. 10.10 show the trace amounts of carbon present in the nanofibers.

The cell studies displayed discharge capacities of 812 and 285 mAh g^{-1}, respectively, for bubble-nanorod-structured Fe_2O_3/C composite nanofibers and hollow bare Fe_2O_3 nanofibers for the 300th cycles at a current density of 1.0 A g^{-1}, and their capacity retentions measured from the second cycle are 84 and 24%, respectively. The initial (first cycle) Coulombic efficiencies of hollow bare Fe_2O_3 nanofibers and bubble-nanorod-structured Fe_2O_3/C composite nanofibers were 81 and 69%, respectively. The initial irreversible capacity loss of the hollow bare Fe_2O_3 nanofibers is ascribed to the formation of an SEI layer on the surface of the nanofibers and the incomplete restoration of metallic Fe into the original oxide during the initial charging process [156, 207]. The high amount of amorphous carbon, which has a low lithium storage capacity and a large initial irreversible capacity loss, decreased the initial discharge capacity and Coulombic efficiency of the bubble-nanorod-structured Fe_2O_3/C composite fibers [208, 209]. The rate capability studies showed that the stable reversible discharge capacities of the bubble-nanorod-structured Fe_2O_3C nanofibers decreased from 913 to 491 mAh g^{-1} as the current density increased

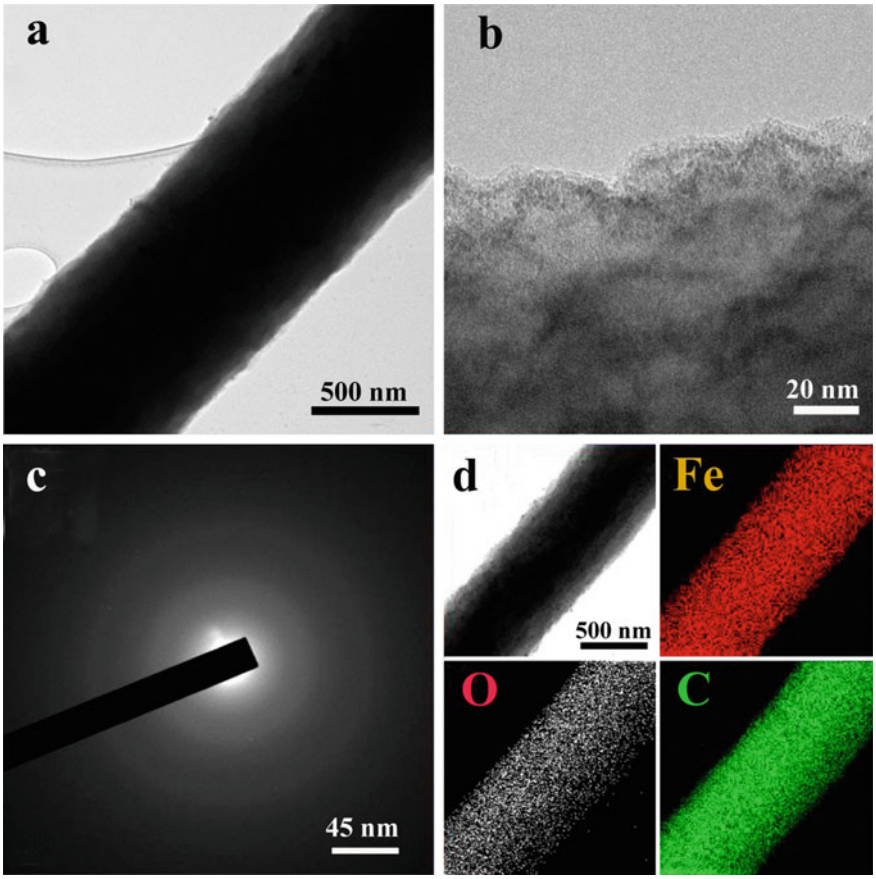

Fig. 10.10 Morphologies, SAED, and elemental mapping images of the nanofibers post-treated at 500 °C under H_2/Ar gas atmosphere: **a**, **b** TEM images, **c** SAED pattern, and **d** elemental mapping. Adapted and reproduced from Ref. [179], Copyright 2015 American Chemical Society

from 0.5 to 5.0 A g^{-1}. Furthermore, the discharge capacity recovered to 852 mAh g^{-1} as the current density was restored to 0.5 A g^{-1}. The electrochemical studies showed that the bubble-nanorod-structured Fe_2O_3C nanofibers showed superior electrochemical properties as an anode material for LIBs as compared with the hollow bare Fe_2O_3 nanofibers. The synergetic effect of hollow nanospheres and a carbon matrix resulted in the superior cycling and rate performance of the bubble-nanorod-structured Fe_2O_3/C nanofibers. The hollow nanospheres accommodate the volume change that occurs during the continuous charge–discharge cycling which leads to the long-term cycling stability. The unique structure of the bubble-nanorod-structured Fe_2O_3/C composite nanofibers results in their superior electrochemical properties by improving the structural stability during long-term cycling.

10.4.1.3 Metal/Fe_2O_4 or Fe_3O_4 Composite Nanofibers

In spite of their lower cost and better safety, the capacity retention of transition metal oxides especially Fe_2O_3/Fe_3O_4 and turning of their energy/power density remain as major drawbacks. However, transition metal oxide spinels (AB_2O_4) with two transition elements (both A- and B-sites) provide the feasibility to tune the energy density and working voltages by varying the transition metal content [210, 211]. Owing to it, zinc [212–215], Co, Cu, etc., have been substituted into iron oxide to construct a ternary metal ferrite ($ZnFe_2O_4$/$CuFe_2O_4$/$CoFe_2O_4$, etc.) and possess a lower working voltage to effectively enhance the total output voltage of the LIBs. $CuFe_2O_4$ nanoparticles, nanorods, and hollow spheres have been fabricated through wet chemical routes, and their electrochemical properties have been investigated [216–218]. Cobalt ferrite ($CoFe_2O_4$) has been well regarded as a distinguished anode due to its low cost, high chemical stability, and good environmental benignity [219–222]. Especially, $CoFe_2O_4$ can deliver a high theoretical capacity of 916 mAh g^{-1} based on an eight-electron conversion reaction. Similarly, zinc ferrite ($ZnFe_2O_4$) generates high capacity as lithium ions form an alloy with Zn and dealloy, while Fe and Zn react with Li_2O to absorb/release Li during lithiation/delithiation. Thus, $ZnFe_2O_4$ implements both conversion [6, 223] and alloy/dealloy [224, 225] reaction, simultaneously. Also, fabrication of nanostructured binary metal oxides could buffer the mechanical strain during the cycling process. In particular, 1D hollow nanostructure could not only provide sufficient void spaces to tolerate the volume change during cycling process, but also allow for efficient electron transport along the longitudinal direction, resulting in the improved electrochemical performance. Hence, $CoFe_2O_4$ nanotubes [226], $CuFe_2O_4$ nanotubes and nanorods [227], $CoFe_2O_4$/C composite fibers [228], interwoven $ZnFe_2O_4$ nanofibers [229], and *N*-doped amorphous carbon-coated Fe_3O_4/SnO_2 coaxial nanofibers [230] were prepared by electrospinning and reported as anode in LIBs having enhanced electrochemical properties. When evaluated as anode materials for LIBs, the $CoFe_2O_4$ nanotubes exhibited good electrochemical performance with high specific capacity of 1228 and 693.9 mAh g^{-1} at a current density of 50 and 200 mA g^{-1}, respectively, long cycling stability over 160 cycles, and good rate capability (214.7 mAh g^{-1} at 2 A g^{-1}) [226], while the $CuFe_2O_4$ nanotubes delivered a high reversible capacity of 1399.4 mAh g^{-1} at a current density of 200 mA·g^{-1} and a capacity retention of ~816 mAh g^{-1} after 50 cycles with a good rate capability (450 mAh g^{-1} at 2.5 A g^{-1}) [227] which is much higher compared to $CoFe_2O_4$ nanotubes (wall thickness of ~50 nm, presented diameters of ~150 nm, and lengths up to several millimeters) [226]. The $CuFe_2O_4$ nanorods showed a discharge capacity of only ~489 mAh g^{-1} after 50 cycles for the same current density of 2.5 A g^{-1} which clearly suggest that the nanotubes have superior electrochemical properties than their counterpart nanotubes [227] which can be attributed to the continuous one-dimensional (1D) hollow nanostructure and their higher surface area. However, compared to $CoFe_2O_4$ nanotubes [226], $CoFe_2O_4$/C composite fibers consist of $CoFe_2O_4$ nanoparticles with a diameter of about 42 nm well dispersed in the carbon matrix as anode material prepared by electrospinning

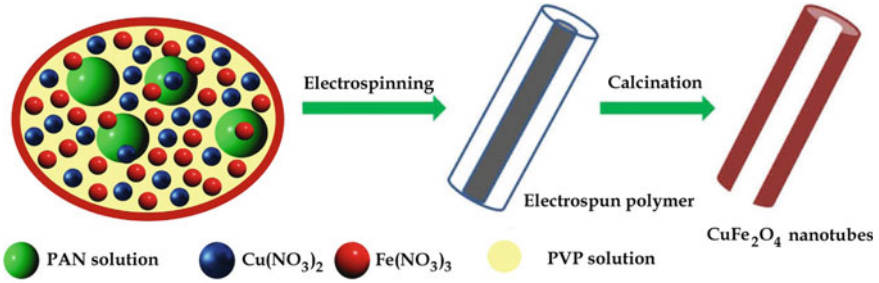

Fig. 10.11 Scheme of the procedure for producing $CuFe_2O_4$ nanotubes. Adapted and reproduced from Ref. [227], Copyright 2014 Elsevier

and thermal technique displayed a stable and reversible capacity of over 490 mAh g^{-1} after 700 cycles at a rate of 2.0 C and good rate capability [228].

The (1D) $CuFe_2O_4$ nanotubes and nanorods were fabricated by a single spinneret electrospinning method followed by thermal decomposition for removal of polymers from the precursor fibers. It was found that phase separation between the electrospun composite materials occurred during the electrospinning process, while the as-spun precursor nanofibers composed of polyacrylonitrile (PAN), polyvinylpyrrolidone (PVP), and metal salts might possess a core–shell structure (PAN as the core and PVP/metal salt composite as the shell) and then transformed to a hollow structure after calcinations as shown in Fig. 10.11 [227]. Based on the literature and the above analysis, the electrochemical reactions involved in the cycling process are believed to proceed as follows:

$$CuFe_2O_4 + nLi + + ne^- \rightarrow Li_nCuFe_2O_4$$
$$Li_nCuFe_2O_4 + (8-n)Li^+ + (8-n) \rightarrow xCu + (2-x)Fe + Fe_xCu(1-x) + 4Li_2O(0 \leq 1 \leq 4)$$
$$Cu + Li_2O \rightarrow CuO + 2Li^+ + 2e^-$$
$$Fe + 3Li_2O \rightarrow Fe_2O_3 + Li^+ + e^-$$

As a heavy metal, Co, is a toxic material, hence nanowebs consisting of interwoven $ZnFe_2O_4$ nanofibers are synthesized by a simple electrospinning technique, to be employed as an environmentally friendly anode in lithium-ion batteries. The morphological studies showed self-assembly of electrospun $ZnFe_2O_4$ nanofibers into intertwined porous nanowebs with a continuous framework. Benefitting from the one-dimensional functional nanostructured architecture, the application of electrospun nanowebs with $ZnFe_2O_4$ nanofiber (ZFO-NF) anodes in LIBs delivers the first charge capacity of 925 mAh g^{-1}, exhibits excellent cyclability, and retains a reversible capacity of 733 mAh g^{-1} up to 30 cycles at 60 mA g^{-1} as compared to $ZnFe_2O_4$ nanorods (ZFO-NR) with a capacity of 200 mAh g^{-1}. The $ZnFe_2O_4$ nanowebs also displayed a high capacity of 400 mAh g^{-1} at 800 mA g^{-1} (1C). The enhanced capacity releases at higher current densities have shown the importance of having

a well-connected electronic wiring during lithium insertion/extraction especially in prolonged cycling [229].

N-doped amorphous carbon-coated Fe_3O_4/SnO_2 coaxial nanofibers were prepared via a facile approach and studied as binder-free self-supported anode for lithium-ion batteries and their electrochemical performance in LIBs. In the process of preparation, the core composite nanofibers were first made by electrospinning technique, and then the shells were conformally coated using the chemical bath deposition and subsequent carbonization using polydopamine as a carbon source (Fig. 10.12). The coaxial nanofibers displayed an enhanced electrochemical storage capacity of 1223,

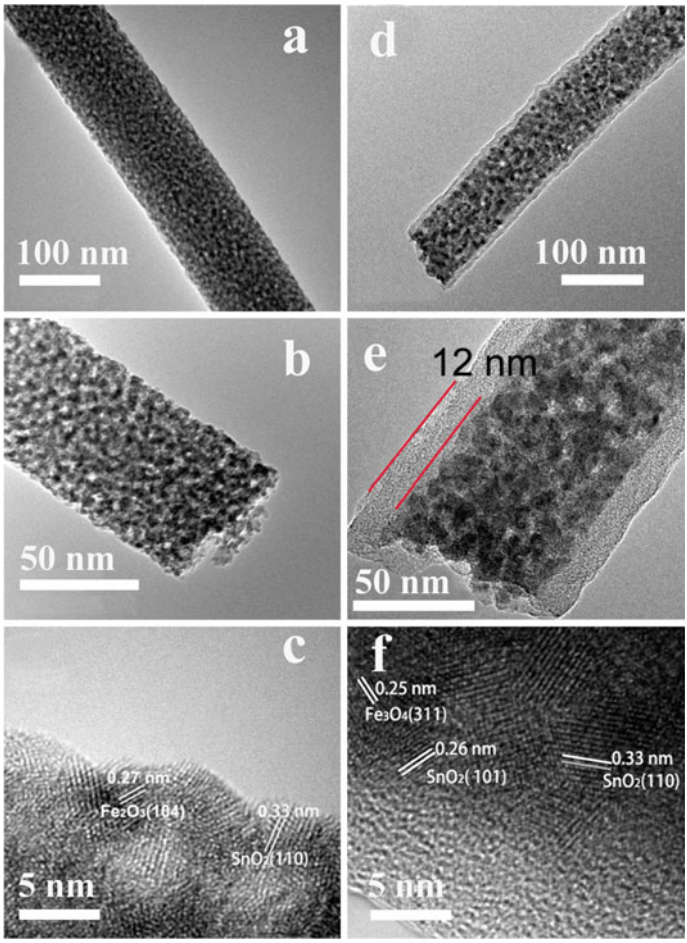

Fig. 10.12 **a**, **b** TEM, **c** high-resolution TEM images of the prepared single Fe_2O_3/SnO_2 composite nanofiber, **d**, **e** TEM, **f** high-resolution TEM images of the carbonized polydopamine-coated single Fe_3O_4/SnO_2 coaxial nanofiber. Adapted and reproduced from Ref. [230]. Copyright 2014 American Chemical Society

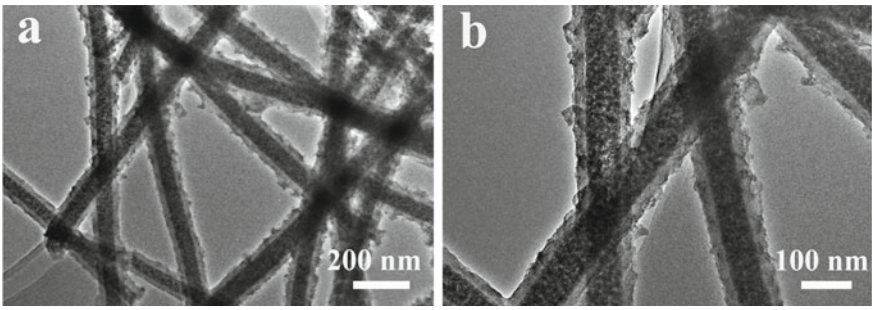

Fig. 10.13 **a**, **b** TEM images of the carbonized polydopamine-coated Fe_3O_4/SnO_2 coaxial nanofibers after rate performance test. Adapted and reproduced from Ref. [230]. Copyright 2014 American Chemical Society

1030, 862, and 640 mAh g^{-1} at 100, 200, 400, and 800 mAg^{-1}, respectively. Even after the current density is increased to 1600 mA g^{-1}, it still maintains a high charge capacity of 402 mAh g^{-1}. When the current density is restored to the initial setting of 100 mA g^{-1}, the carbonized polydopamine-coated Fe_3O_4/SnO_2 coaxial nanofiber electrode (Fig. 10.13) leads to a reversible capacity of 1070 mAh g^{-1} displaying not only its superior capacity retention but also excellent capacity recovery performance. Also, it was found that the morphology of the interwoven nanofibers was maintained even after the rate cycle test. The superior electrochemical performance originates from the structural stability of the N-doped amorphous carbon shells formed by carbonizing polydopamine [230]. On the basis of the literature, the electrochemical reactions of the carbonized polydopamine-coated Fe_3O_4/SnO_2 coaxial nanofibers can be described as follows

$$SnO_2 + 4Li^+ + 4e^- \rightarrow Sn + 2LiO$$
$$Sn + xLi^+ + xe^- \rightarrow Li_xSn(0 \leq x \leq 4.4)$$
$$Fe_3O_4 + 8Li^+ + 8e^- \rightarrow 3Fe + 4Li_2O$$

10.5 Conclusion

For the achievement of best performing lithium-ion batteries, different materials were greatly explored that can deliver a best performing system. Metal oxides possess great significance in lithium-ion batteries since they are capable of exhibiting better electrochemical properties. Similar to carbon base materials, currently, metal oxides are also widely explored as anodes in LIBs. Iron oxide-based anode materials such as Fe_2O_3 and Fe_3O_4 are promising due to its high capacity and lithium storage properties. Even though, despite of its high capacity, the poor cycling stability and high polarization during lithiation and delithiation process limit its practical use in LIBs.

Modifications of structural and surface characteristics are considered to be the best method for the enhancement of electrochemical properties of these anodes. Electrospinning is considered to be the best method for this. Electrospinning is considered to be the most versatile and simple method that provides a flexible platform for the fabrication of nanostructures that can deliver better battery performance. Porous and hollow iron oxide structure results by the electrospinning technique facilitate the fast lithium-ion transfer as well as it accommodates the volume change that results in unique electrochemical properties. Similarly, the hollow nanotubes and nanorods that results by this technique can deliver high performance in battery owing to its high surface area, controlled shape, and a low density. Further performance can be enhanced by the structural modification by incorporating different metals to form the composite structures which can result an enhancement in conductivity which is significant for a better performing electrode material. These potential features make iron oxide-based materials as the best performing anode material in LIBs.

References

1. Nam KT, Kim DW, Yoo PJ et al (2006) Virus-enabled synthesis and assembly of nanowires for lithium ion battery electrodes. Science 312(80):885–888. https://doi.org/10.1126/science.1122716
2. Zhang H, Yu X, Braun PV (2011) Three-dimensional bicontinuous ultrafast-charge and-discharge bulk battery electrodes. Nat Nanotechnol 6:277–281. https://doi.org/10.1038/nnano.2011.38
3. Wang H, Yang Y, Liang Y et al (2011) $LiMn_1$-x$FexPO_4$ nanorods grown on graphene sheets for ultrahigh-rate-performance lithium ion batteries. Angew Chemie Int Ed 50:7364–7368. https://doi.org/10.1002/anie.201103163
4. Hwang TH, Lee YM, Kong BS et al (2012) Electrospun core-shell fibers for robust silicon nanoparticle-based lithium ion battery anodes. Nano Lett 12:802–807. https://doi.org/10.1021/nl203817r
5. O'Heir J (2017) Building better batteries. Mech Eng 139:10–11. https://doi.org/10.1038/451652a
6. Poizot P, Laruelle S, Grugeon S et al (2000) Nano-sized transition-metal oxides as negative-electrode materials for lithium-ion batteries. Nature 407:496–499. https://doi.org/10.1038/35035045
7. Lou XW, Deng D, Lee JY et al (2008) Self-supported formation of needlelike Co_3O_4 nanotubes and their application as lithium-ion battery electrodes. Adv Mater 20:258–262. https://doi.org/10.1002/adma.200702412
8. Xiong S, Chen JS, Lou XW, Zeng HC (2012) Mesoporous Co_3O_4 and CoO@C topotactically transformed from chrysanthemum-like $Co(CO_3)0.5(OH)\cdot 0.11H_2O$ and their lithium-storage properties. Adv Funct Mater 22:861–871. https://doi.org/10.1002/adfm.201102192
9. Lang L, Xu Z (2013) In situ synthesis of porous Fe_3O_4/C microbelts and their enhanced electrochemical performance for lithium-ion batteries. ACS Appl Mater Interfaces 5:1698–1703. https://doi.org/10.1021/am302753p
10. Li Y, Tan B, Wu Y (2006) Freestanding mesoporous quasi-single-crystalline Co_3O_4 nanowire arrays. J Am Chem Soc 128:14258–14259. https://doi.org/10.1021/ja065308q
11. Xiong QQ, Tu JP, Lu Y et al (2012) Three-dimensional porous nano-Ni/Fe_3O_4 composite film: Enhanced electrochemical performance for lithium-ion batteries. J Mater Chem 22:18639–18645. https://doi.org/10.1039/c2jm33770c

12. Chaudhari S, Srinivasan M (2012) 1D hollow α-Fe_2O_3 electrospun nanofibers as high performance anode material for lithium ion batteries. J Mater Chem 22:23049–23056. https://doi.org/10.1039/c2jm32989a
13. Wang B, Chen JS, Bin WuH et al (2011) Quasiemulsion-templated formation of α-Fe_2O_3 hollow spheres with enhanced lithium storage properties. J Am Chem Soc 133:17146–17148. https://doi.org/10.1021/ja208346s
14. Zhong J, Cao C, Liu Y et al (2010) Hollow core-shell η-Fe_2O_3 microspheres with excellent lithium-storage and gas-sensing properties. Chem Commun 46:3869–3871. https://doi.org/10.1039/c0cc00204f
15. Xiong QQ, Tu JP, Lu Y et al (2012) Synthesis of hierarchical hollow-structured single-crystalline magnetite (Fe_3O_4) microspheres: the highly powerful storage versus lithium as an anode for lithium ion batteries. J Phys Chem C 116:6495–6502. https://doi.org/10.1021/jp3002178
16. Chen J, Xu L, Li W, Gou X (2005) α-Fe_2O_3 nanotubes in gas sensor and lithium-ion battery applications. Adv Mater 17:582–586. https://doi.org/10.1002/adma.200401101
17. Xu JS, Zhu YJ (2012) Monodisperse Fe 3O 4 and γ-Fe_2O_3 magnetic mesoporous microspheres as anode materials for lithium-ion batteries. ACS Appl Mater Interfaces 4:4752–4757. https://doi.org/10.1021/am301123f
18. Li J, Wan W, Zhou H et al (2011) Hydrothermal synthesis of TiO_2(B) nanowires with ultrahigh surface area and their fast charging and discharging properties in Li-ion batteries. Chem Commun 47:3439–3441. https://doi.org/10.1039/c0cc04634e
19. Wang K, Wei M, Morris MA et al (2007) Mesoporous titania nanotubes: their preparation and application as electrode materials for rechargeable lithium batteries. Adv Mater 19:3016–3020. https://doi.org/10.1002/adma.200602189
20. Sayle TXT, Maphanga RR, Ngoepe PE, Sayle DC (2009) Predicting the electrochemical properties of MnO_2 nanomaterials used in rechargeable Li batteries: simulating nanostructure at the atomistic level. J Am Chem Soc 131:6161–6173. https://doi.org/10.1021/ja8082335
21. Jiao F, Bruce PG (2007) Mesoporous crystalline β-MnO_2—a reversible positive electrode for rechargeable lithium batteries. Adv Mater 19:657–660. https://doi.org/10.1002/adma.200602499
22. Zhao J, Tao Z, Liang J, Chen J (2008) Facile synthesis of nanoporous γ-MnO_2 structures and their application in rechargeable Li-ion batteries. Cryst Growth Des 8:2799–2805. https://doi.org/10.1021/cg701044b
23. Meduri P, Pendyala C, Kumar V et al (2009) Hybrid tin oxide nanowires as stable and high capacity anodes for li-ion batteries. Nano Lett 9:612–616. https://doi.org/10.1021/n1802864a
24. Deng D, Lee JY (2008) Hollow core-shell mesospheres of crystalline SnO_2 nanoparticle aggregates for high capacity Li+ ion storage. Chem Mater 20:1841–1846. https://doi.org/10.1021/cm7030575
25. Ye J, Zhang H, Yang R et al (2010) Morphology-controlled synthesis of SnO2 nanotubes by using 1D silica mesostructures as sacrificial templates and their applications in lithium-ion batteries. Small 6:296–306. https://doi.org/10.1002/smll.200901815
26. Balogun MS, Wu Z, Luo Y et al (2016) High power density nitridated hematite (α-Fe2O3) nanorods as anode for high-performance flexible lithium ion batteries. J Power Sources 308:7–17. https://doi.org/10.1016/j.jpowsour.2016.01.043
27. Song Y, Qin S, Zhang Y et al (2010) Large-scale porous hematite nanorod arrays: Direct growth on titanium foil and reversible lithium storage. J Phys Chem C 114:21158–21164. https://doi.org/10.1021/jp1091009
28. Brandt A, Balducci A (2013) A study about the use of carbon coated iron oxide-based electrodes in lithium-ion capacitors. Electrochim Acta 108:219–225. https://doi.org/10.1016/j.electacta.2013.06.076
29. Taberna PL, Mitra S, Poizot P et al (2006) High rate capabilities Fe3O4-based Cu nano-architectured electrodes for lithium-ion battery applications. Nat Mater 5:567–573. https://doi.org/10.1038/nmat1672

30. Behera SK (2011) Facile synthesis and electrochemical properties of Fe3O 4 nanoparticles for Li ion battery anode. J Power Sources 196:8669–8674. https://doi.org/10.1016/j.jpowsour.2011.06.067
31. Bruck AM, Cama CA, Gannett CN et al (2016) Nanocrystalline iron oxide based electroactive materials in lithium ion batteries: the critical role of crystallite size, morphology, and electrode heterostructure on battery relevant electrochemistry. Inorg Chem Front 3:26–40. https://doi.org/10.1039/c5qi00247h
32. Wu LL, Zhao DL, Cheng XW et al (2017) Nanorod Mn3O4 anchored on graphene nanosheet as anode of lithium ion batteries with enhanced reversible capacity and cyclic performance. J Alloys Compd 728:383–390. https://doi.org/10.1016/j.jallcom.2017.09.005
33. Zeng S, Tang K, Li T et al (2008) Facile route for the fabrication of porous hematite nanoflowers: Its synthesis, growth mechanism, application in the lithium ion battery, and magnetic and photocatalytic properties. J Phys Chem C 112:4836–4843. https://doi.org/10.1021/jp0768773
34. Reddy MV, Yu T, Sow CH et al (2007) α-Fe2O3 nanoflakes as an anode material for li-ion batteries. Adv Funct Mater 17:2792–2799. https://doi.org/10.1002/adfm.200601186
35. Morales J, Sánchez L, Martín F et al (2005) Synthesis and characterization of nanometric iron and iron-titanium oxides by mechanical milling: Electrochemical properties as anodic materials in lithium cells. J Electrochem Soc 152:1748–1754. https://doi.org/10.1149/1.1972812
36. Muraliganth T, Vadivel Murugan A, Manthiram A (2009) Facile synthesis of carbon-decorated single-crystalline Fe3 O4 nanowires and their application as high performance anode in lithium ion batteries. Chem Commun 7360–7362. https://doi.org/10.1039/b916376j
37. Magasinski A, Dixon P, Hertzberg B et al (2010) Erratum: high-performance lithium-ion anodes using a hierarchical bottom-up approach. Nat Mater 9:353–358. https://doi.org/10.1038/nmat2749
38. Guo B, Fang X, Li B et al (2012) Synthesis and lithium storage mechanism of ultrafine MoO 2 nanorods. Chem Mater 24:457–463. https://doi.org/10.1021/cm202459r
39. Zhou G, Wang DW, Li F et al (2010) Graphene-wrapped Fe_3O_4 anode material with improved reversible capacity and cyclic stability for lithium ion batteries. Chem Mater 22:5306–5313. https://doi.org/10.1021/cm101532x
40. Gu M, Li Y, Li X et al (2012) In situ TEM study of lithiation behavior of silicon nanoparticles attached to and embedded in a carbon matrix. ACS Nano 6:8439–8447. https://doi.org/10.1021/nn303312m
41. Wang H, Cui LF, Yang Y et al (2010) Mn_3O_4-graphene hybrid as a high-capacity anode material for lithium ion batteries. J Am Chem Soc 132:13978–13980. https://doi.org/10.1021/ja105296a
42. Ban C, Wu Z, Gillaspie DT et al (2010) Nanostructured Fe_3O_4/SWNT electrode: Binder-free and high-rate Li-ion anode. Adv Mater 22:145–149. https://doi.org/10.1002/adma.200904285
43. Yoon T, Chae C, Sun YK et al (2011) Bottom-up in situ formation of Fe_3O_4 nanocrystals in a porous carbon foam for lithium-ion battery anodes. J Mater Chem 21:17325–17330. https://doi.org/10.1039/c1jm13450g
44. Li Y, Zhu S, Liu Q et al (2012) Carbon-coated SnO_2@C with hierarchically porous structures and graphite layers inside for a high-performance lithium-ion battery. J Mater Chem 22:2766–2773. https://doi.org/10.1039/c1jm14290a
45. Kang E, Jung YS, Cavanagh AS et al (2011) Fe_3O_4 nanoparticles confined in mesocellular carbon foam for high performance anode materials for lithium-ion batteries. Adv Funct Mater 21:2430–2438. https://doi.org/10.1002/adfm.201002576
46. Li B, Cao H, Shao J, Qu M (2011) Enhanced anode performances of the Fe_3O_4-Carbon-rGO three dimensional composite in lithium ion batteries. Chem Commun 47:10374–10376. https://doi.org/10.1039/c1cc13462k
47. Piao Y, Kim HS, Sung YE, Hyeon T (2010) Facile scalable synthesis of magnetite nanocrystals embedded in carbon matrix as superior anode materials for lithium-ion batteries. Chem Commun 46:118–120. https://doi.org/10.1039/b920037a

48. Li H, Zhou H (2012) Enhancing the performances of Li-ion batteries by carbon-coating: present and future. Chem Commun 48:1201–1217. https://doi.org/10.1039/c1cc14764a
49. Zhu T, Chen JS, Lou XW (2011) Glucose-assisted one-pot synthesis of FeOOH nanorods and their transformation to Fe_3O_4@carbon nanorods for application in lithium ion batteries. J Phys Chem C 115:9814–9820. https://doi.org/10.1021/jp2013754
50. Zhang XF, Wang KX, Wei X, Chen JS (2011) Carbon-coated V_2O_5 nanocrystals as high performance cathode material for lithium ion batteries. Chem Mater 23:5290–5292. https://doi.org/10.1021/cm202812z
51. Chen D, Ji G, Ma Y et al (2011) Graphene-encapsulated hollow Fe_3O_4 nanoparticle aggregates as a high-performance anode material for lithium ion batteries. ACS Appl Mater Interfaces 3:3078–3083. https://doi.org/10.1021/am200592r
52. Chen JS, Zhang Y, Lou XW (2011) One-pot synthesis of uniform Fe_3O_4 nanospheres with carbon matrix support for improved lithium storage capabilities. ACS Appl Mater Interfaces 3:3276–3279. https://doi.org/10.1021/am201079z
53. Zhao X, Xia D, Zheng K (2012) Fe_3O_4/Fe/carbon composite and its application as anode material for lithium-ion batteries. ACS Appl Mater Interfaces 4:1350–1356. https://doi.org/10.1021/am201617j
54. Wu J, Qin X, Miao C et al (2016) A honeycomb-cobweb inspired hierarchical core-shell structure design for electrospun silicon/carbon fibers as lithium-ion battery anodes. Carbon N Y 98:582–591. https://doi.org/10.1016/j.carbon.2015.11.048
55. Bonino CA, Ji L, Lin Z et al (2011) Electrospun carbon-tin oxide composite nanofibers for use as lithium ion battery anodes. ACS Appl Mater Interfaces 3:2534–2542. https://doi.org/10.1021/am2004015
56. Kong J, Tan HR, Tan SY et al (2010) A generic approach for preparing core-shell carbon-metal oxide nanofibers: morphological evolution and its mechanism. Chem Commun 46:8773–8775. https://doi.org/10.1039/c0cc03006f
57. Tran T, McCormac K, Li J et al (2014) Electrospun SnO_2 and TiO_2 composite nanofibers for lithium ion batteries. Electrochim Acta 117:68–75. https://doi.org/10.1016/j.electacta.2013.11.101
58. Zhou D, Song WL, Fan LZ (2015) Hollow core-shell SnO_2/C fibers as highly stable anodes for lithium-ion batteries. ACS Appl Mater Interfaces 7:21472–21478. https://doi.org/10.1021/acsami.5b06512
59. Li X, Zhang H, Feng C et al (2014) Novel cage-like α-Fe_2O_3/SnO_2 composite nanofibers by electrospinning for rapid gas sensing properties. RSC Adv 4:27552–27555. https://doi.org/10.1039/c4ra03307h
60. Wang X, Zhang K, Zhu M et al (2008) Continuous polymer nanofiber yarns prepared by self-bundling electrospinning method. Polymer (Guildf) 49:2755–2761. https://doi.org/10.1016/j.polymer.2008.04.015
61. Fei L, Williams BP, Yoo SH et al (2016) Graphene folding in si rich carbon nanofibers for highly stable, high capacity Li-ion battery anodes. ACS Appl Mater Interfaces 8:5243–5250. https://doi.org/10.1021/acsami.5b10548
62. Wang HG, Yuan S, Ma DL et al (2015) Electrospun materials for lithium and sodium rechargeable batteries: from structure evolution to electrochemical performance. Energy Environ Sci 8:1660–1681. https://doi.org/10.1039/c4ee03912b
63. Xu Y, Zhu Y, Han F et al (2015) 3D Si/C fiber paper electrodes fabricated using a combined electrospray/electrospinning technique for Li-ion batteries. Adv Energy Mater 5:1–7. https://doi.org/10.1002/aenm.201400753
64. Zhang M, Yan F, Tang X et al (2014) Flexible CoO-graphene-carbon nanofiber mats as binder-free anodes for lithium-ion batteries with superior rate capacity and cyclic stability. J Mater Chem A 2:5890–5897. https://doi.org/10.1039/c4ta00311j
65. Zhao B, Cai R, Jiang S et al (2012) Highly flexible self-standing film electrode composed of mesoporous rutile TiO_2/C nanofibers for lithium-ion batteries. Electrochim Acta 85:636–643. https://doi.org/10.1016/j.electacta.2012.08.126

66. Miao YE, Wang R, Chen D et al (2012) Electrospun self-standing membrane of hierarchical SiO 2atγ-AlOOH (Boehmite) core/sheath fibers for water remediation. ACS Appl Mater Interfaces 4:5353–5359. https://doi.org/10.1021/am3012998
67. McCann JT, Marquez M, Xia Y (2006) Highly porous fibers by electrospinning into a cryogenic liquid. J Am Chem Soc 128:1436–1437. https://doi.org/10.1021/ja056810y
68. Mou F, Guan JG, Shi W et al (2010) Oriented contraction: a facile nonequilibrium heat-treatment approach for fabrication of maghemite fiber-in-tube and tube-in-tube nanostructures. Langmuir 26:15580–15585. https://doi.org/10.1021/la102830p
69. Chen H, Wang N, Di J et al (2010) Nanowire-in-microtube structured core/shell fibers via multifluidic coaxial electrospinning. Langmuir 26:11291–11296. https://doi.org/10.1021/la100611f
70. Zhu C, Yu Y, Gu L et al (2011) Electrospinning of highly electroactive carbon-coated single-crystalline $LiFePO_4$ nanowires. Angew Chemie Int Ed 50:6278–6282. https://doi.org/10.1002/anie.201005428
71. McCann JT, Lim B, Ostermann R et al (2007) Carbon nanotubes by electrospinning with a polyelectrolyte and vapor deposition polymerization. Nano Lett 7:2470–2474. https://doi.org/10.1021/nl071234k
72. Reports and data, lithium ion battery market to reach USD 109.72 Billion By 2026 (2019)
73. Bhutani A, Schiller JA, Zuo JL et al (2017) Combined computational and in situ experimental search for phases in an open ternary system, Ba-Ru-S. Chem Mater 29:5841–5849. https://doi.org/10.1021/acs.chemmater.7b00809
74. Whittingham BMS (2012) WhittinghamIEEE2012energystorage.pdf. 100
75. Mehul Oswal JP, RZ A comparative study of Lithium-Ion Batteries
76. Haruyama J, Sodeyama K, Han L et al (2014) Space-charge layer effect at interface between oxide cathode and sulfide electrolyte in all-solid-state lithium-ion battery. Chem Mater 26:4248–4255. https://doi.org/10.1021/cm5016959
77. Kim Y (2012) Lithium nickel cobalt manganese oxide synthesized using alkali chloride flux: Morphology and performance as a cathode material for lithium ion batteries. ACS Appl Mater Interfaces 4:2329–2333. https://doi.org/10.1021/am300386j
78. Chen Y, Lu Z, Zhou L et al (2012) Triple-coaxial electrospun amorphous carbon nanotubes with hollow graphitic carbon nanospheres for high-performance Li ion batteries. Energy Environ Sci 5:7898–7902. https://doi.org/10.1039/c2ee22085g
79. Date I (2009) This document is downloaded from DR-NTU, Nanyang Technological. Security 299:1719–1722. https://doi.org/10.1063/1.2978249
80. Wang J, Li L, Wong CL et al (2013) Controlled synthesis of α-FeOOH nanorods and their transformation to mesoporous α-Fe_2O_3, Fe_3O_4@C nanorods as anodes for lithium ion batteries. RSC Adv 3:15316–15326. https://doi.org/10.1039/c3ra41886c
81. Chagnes A, Swiatowsk J (2012) Electrolyte and solid-electrolyte interphase layer in lithium-ion batteries. Lithium Ion Batter New Dev. https://doi.org/10.5772/31112
82. Zhang HP, Zhang P, Li ZH, Sun M, Wu YP, Wu HQ (2007) A novel sandwiched membrane as polymer electrolyte for lithium ion battery. Electrochem Commun 9(7):1700–1703
83. Chapman N (2016) Spectroscopic measurements of ionic associaition in common lithium salts and carbonate electrolytes. https://doi.org/10.23860/thesis-chapman-navid-2016
84. Scrosati B, Croce F, Persi L (2000) Impedance spectroscopy study of PEO-based nanocomposite polymer electrolytes. J Electrochem Soc 147:1718–1721. https://doi.org/10.1149/1.1393423
85. Shin JH, Henderson WA, Passerini S (2005) PEO-based polymer electrolytes with ionic liquids and their use in lithium metal-polymer electrolyte batteries. J Electrochem Soc 152:978–983. https://doi.org/10.1149/1.1890701
86. Gopalan AI, Santhosh P, Manesh KM et al (2008) Development of electrospun PVdF-PAN membrane-based polymer electrolytes for lithium batteries. J Memb Sci 325:683–690. https://doi.org/10.1016/j.memsci.2008.08.047
87. Newcomb BA, Chae HG, Gulgunje PV et al (2014) Stress transfer in polyacrylonitrile/carbon nanotube composite fibers. Polymer (Guildf) 55:2734–2743. https://doi.org/10.1016/j.polymer.2014.04.008

88. Kim JR, Choi SW, Jo SM et al (2004) Electrospun PVdF-based fibrous polymer electrolytes for lithium ion polymer batteries. Electrochim Acta 50:69–75. https://doi.org/10.1016/j.electacta.2004.07.014
89. Mohamed NS, Arof AK (2004) Investigation of electrical and electrochemical properties of PVDF-based polymer electrolytes. J Power Sources 132:229–234. https://doi.org/10.1016/j.jpowsour.2003.12.031
90. Angulakshmi N, Thomas S, Nahm KS et al (2011) Electrochemical and mechanical properties of nanochitin-incorporated PVDF-HFP-based polymer electrolytes for lithium batteries. Ionics (Kiel) 17:407–414. https://doi.org/10.1007/s11581-010-0517-z
91. Stephan AM, Nahm KS, Anbu Kulandainathan M et al (2006) Poly(vinylidene fluoride-hexafluoropropylene) (PVdF-HFP) based composite electrolytes for lithium batteries. Eur Polym J 42:1728–1734. https://doi.org/10.1016/j.eurpolymj.2006.02.006
92. Chiu CY, Yen YJ, Kuo SW et al (2007) Complicated phase behavior and ionic conductivities of PVP-co-PMMA-based polymer electrolytes. Polymer (Guildf) 48:1329–1342. https://doi.org/10.1016/j.polymer.2006.12.059
93. Rajendran S, Kannan R, Mahendran O (2001) An electrochemical investigation on PMMA/PVdF blend-based polymer electrolytes. Mater Lett 49:172–179. https://doi.org/10.1016/S0167-577X(00)00363-3
94. Doughty DH, Butler PC, Akhil AA, Clark NH, Boyes JD (2010) Batteries for large-scale stationary electrical energy storage. Electrochem Soc Interface 19(3):49
95. Corporation LB, Beach N (1999) Laub BioChem. Computer (Long Beach Calif) 18:461–472. https://doi.org/10.1016/0025-5408(83)90138-1
96. Chitra S, Kalyani P, Mohan T et al (1999) Characterization and electrochemical studies of LiMn2O4 cathode materials prepared by combustion method. J Electroceramics 3:433–441. https://doi.org/10.1023/A:1009982301437
97. Li X, Cheng F, Guo B, Chen J (2005) Template-synthesized $LiCoO_2$, $LiMn_2O_4$, and LiNi0.8Co0.2O2 nanotubes as the cathode materials of lithium ion batteries. J Phys Chem B 109:14017–14024. https://doi.org/10.1021/jp051900a
98. Tarascon JM, Armand M (2011) Issues and challenges facing rechargeable lithium batteries. In: Materials for sustainable energy: a collection of peer-reviewed research and review articles from Nature Publishing Group, pp. 171–179. https://doi.org/10.1038/35104644
99. Goodenough JB, Park KS (2013) The Li-ion rechargeable battery: a perspective. J Am Chem Soc 135:1167–1176. https://doi.org/10.1021/ja3091438
100. Nitta N, Wu F, Lee JT, Yushin G (2015) Li-ion battery materials: present and future. Mater Today 18:252–264. https://doi.org/10.1016/j.mattod.2014.10.040
101. Etacheri V, Marom R, Elazari R et al (2011) Challenges in the development of advanced Li-ion batteries: a review. Energy Environ Sci 4:3243–3262. https://doi.org/10.1039/c1ee01598b
102. Mizushima K, Jones PC, Wiseman PJ, Goodenough JB (1981) $LixCoO_2$ (0 < x~l): A new cathode material for batteries of high energy density K. Solid State Ionics 3–4:171–174. https://doi.org/10.1016/0167-2738(81)90077-1
103. Endo M, Nakamura JI, Sasabe Y, Takahashi T, Inagaki M (1995) Lithium secondary battery using vapor grown carbon fibers as a negative electrode and analysis of the electrode mechanism by TEM observation. IEEJ Trans Fundam Mater 115(4):349–356
104. Liu H, Yang Y, Zhang J (2007) Reaction mechanism and kinetics of lithium ion battery cathode material $LiNiO_2$ with CO_2. J Power Sources 173:556–561. https://doi.org/10.1016/j.jpowsour.2007.04.083
105. Kim TH, Park JS, Chang SK et al (2012) The current move of lithium ion batteries towards the next phase. Adv Energy Mater 2:860–872. https://doi.org/10.1002/aenm.201200028
106. Shaju KM, Subba Rao GV, Chowdari BVR (2002) Performance of layered $Li(Ni1/3Co1/3Mn1/3)O_2$ as cathode for Li-ion batteries. Electrochim Acta 48:145–151. https://doi.org/10.1016/S0013-4686(02)00593-5
107. Koyama Y, Makimura Y, Tanaka I et al (2004) Systematic research on insertion materials based on superlattice models in a phase triangle of $LiCoO_2$-$LiNiO_2$-$LiMnO_2$ I. First-principles

calculation on electronic and crystal structures, phase stability and new LiNi1/2Mn1/2O_2 material. J Electrochem Soc 151:1499–1506. https://doi.org/10.1149/1.1783908
108. Park OK, Cho Y, Lee S et al (2011) Who will drive electric vehicles, olivine or spinel? Energy Environ Sci 4:1621–1633. https://doi.org/10.1039/c0ee00559b
109. Myung ST, Maglia F, Park KJ et al (2017) Nickel-rich layered cathode materials for automotive lithium-ion batteries: achievements and perspectives. ACS Energy Lett 2:196–223. https://doi.org/10.1021/acsenergylett.6b00594
110. Yamada A, Chung SC, Hinokuma K (2001) Optimized $LiFePO_4$ for lithium battery cathodes. J Electrochem Soc 148:224–229. https://doi.org/10.1149/1.1348257
111. Huang ZD, Oh SW, He YB et al (2012) Porous C-$LiFePO_4$-C composite microspheres with a hierarchical conductive architecture as a high performance cathode for lithium ion batteries. J Mater Chem 22:19643–19645. https://doi.org/10.1039/c2jm33960a
112. Shen L, Uchaker E, Zhang X, Cao G (2012) Hydrogenated $Li_4Ti_5O_{12}$ nanowire arrays for high rate lithium ion batteries. Adv Mater 24:6502–6506. https://doi.org/10.1002/adma.201203151
113. Liu Y, Wang YM, Yakobson BI, Wood BC (2014) Assessing carbon-based anodes for lithium-ion batteries: a universal description of charge-transfer binding. Phys Rev Lett 113. https://doi.org/10.1103/PhysRevLett.113.028304
114. Goriparti S, Miele E, De Angelis F et al (2014) Review on recent progress of nanostructured anode materials for Li-ion batteries. J Power Sources 257:421–443. https://doi.org/10.1016/j.jpowsour.2013.11.103
115. Lian P, Zhu X, Liang S et al (2010) Large reversible capacity of high quality graphene sheets as an anode material for lithium-ion batteries. Electrochim Acta 55:3909–3914. https://doi.org/10.1016/j.electacta.2010.02.025
116. Zhang B, Xu ZL, He YB et al (2014) Exceptional rate performance of functionalized carbon nanofiber anodes containing nanopores created by (Fe) sacrificial catalyst. Nano Energy 4:88–96. https://doi.org/10.1016/j.nanoen.2013.12.011
117. Raccichini R, Varzi A, Passerini S, Scrosati B (2015) The role of graphene for electrochemical energy storage. Nat Mater 14:271–279. https://doi.org/10.1038/nmat4170
118. Liu C, Li F, Lai-Peng M, Cheng HM (2010) Advanced materials for energy storage. Adv Mater 22:28–62. https://doi.org/10.1002/adma.200903328
119. Kim J, Zhou H, Hosono E et al (2008) Large reversible Li storage of graphene nanosheet families for use in rechargeable lithium ion batteries. Nano Lett 8:2277–2282. https://doi.org/10.1021/nl800957b
120. Klein F, Jache B, Bhide A, Adelhelm P (2013) Conversion reactions for sodium-ion batteries. Phys Chem Chem Phys 15:15876–15887. https://doi.org/10.1039/c3cp52125g
121. Cabana J, Monconduit L, Larcher D, Palacín MR (2010) Beyond intercalation-based Li-ion batteries: the state of the art and challenges of electrode materials reacting through conversion reactions. Adv Mater 22:170–192. https://doi.org/10.1002/adma.201000717
122. Online VA, Afrooz M (2015) RSC Adv. https://doi.org/10.1039/b000000x
123. Zhou W, Zhu J, Cheng C et al (2011) A general strategy toward graphene@metal oxide core-shell nanostructures for high-performance lithium storage. Energy Environ Sci 4:4954–4961. https://doi.org/10.1039/c1ee02168k
124. Aravindan V, Lee YS, Madhavi S (2017) Best practices for mitigating irreversible capacity loss of negative electrodes in Li-ion batteries. Adv Energy Mater 7:1–17. https://doi.org/10.1002/aenm.201602607
125. Lu J, Chen Z, Pan F, Cui Y, Amine K (2018) High-performance anode materials for rechargeable lithium-ion batteries. Electrochemi Energy Rev 1(1):35–53
126. Yoo H, Lee JI, Kim H et al (2011) Helical silicon/silicon oxide core-shell anodes grown onto the surface of bulk silicon. Nano Lett 11:4324–4328. https://doi.org/10.1021/nl202417c
127. Yin YX, Wan LJ, Guo YG (2012) Silicon-based nanomaterials for lithium-ion batteries. Chinese Sci Bull 57:4104–4110. https://doi.org/10.1007/s11434-012-5017-2
128. Wang B, Luo B, Li X, Zhi L (2012) The dimensionality of Sn anodes in Li-ion batteries. Mater Today 15:544–552. https://doi.org/10.1016/S1369-7021(13)70012-9

129. Obrovac MN, Chevrier VL (2014) Alloy negative electrodes for Li-ion batteries. Chem Rev 114:11444–11502. https://doi.org/10.1021/cr500207g
130. Jin S, Deng H, Long D et al (2011) Facile synthesis of hierarchically structured Fe_3O 4/carbon micro-flowers and their application to lithium-ion battery anodes. J Power Sources 196:3887–3893. https://doi.org/10.1016/j.jpowsour.2010.12.078
131. Lee JE, Yu SH, Lee DJ et al (2012) Facile and economical synthesis of hierarchical carbon-coated magnetite nanocomposite particles and their applications in lithium ion battery anodes. Energy Environ Sci 5:9528–9533. https://doi.org/10.1039/c2ee22792d
132. Zhou G, Wang DW, Hou PX et al (2012) A nanosized Fe 2 O 3 decorated single-walled carbon nanotube membrane as a high-performance flexible anode for lithium ion batteries. J Mater Chem 22:17942–17946. https://doi.org/10.1039/c2jm32893c
133. Li Y, Zhu C, Lu T et al (2013) Simple fabrication of a Fe2O3/carbon composite for use in a high-performance lithium ion battery. Carbon N Y 52:565–573. https://doi.org/10.1016/j.carbon.2012.10.015
134. Chou SL, Wang JZ, Wexler D et al (2010) High-surface-area α-Fe_2O_3/carbon nanocomposite: one-step synthesis and its highly reversible and enhanced high-rate lithium storage properties. J Mater Chem 20:2092–2098. https://doi.org/10.1039/b922237e
135. Yoon T, Kim J, Kim J, Lee JK (2013) Electrostatic self-assembly of Fe_3O_4 nanoparticles on graphene oxides for high capacity lithium-ion battery anodes. Energies 6:4830–4840. https://doi.org/10.3390/en6094830
136. Xu L, Tian Y, Liu T et al (2018) α-Fe_2O_3 nanoplates with superior electrochemical performance for lithium-ion batteries. Green Energy Environ 3:156–162. https://doi.org/10.1016/j.gee.2018.01.005
137. Vetter J, Novák P, Wagner MR et al (2005) Ageing mechanisms in lithium-ion batteries. J Power Sources 147:269–281. https://doi.org/10.1016/j.jpowsour.2005.01.006
138. Chan CK, Peng H, Liu G et al (2008) High-performance lithium battery anodes using silicon nanowires. Nat Nanotechnol 3:31–35. https://doi.org/10.1038/nnano.2007.411
139. Martinet S (2016) Nanomaterials for rechargeable lithium batteries. Nanosci Technol 471–512. https://doi.org/10.1007/978-3-319-32023-6_13
140. Ji L, Lin Z, Alcoutlabi M, Zhang X (2011) Recent developments in nanostructured anode materials for rechargeable lithium-ion batteries. Energy Environ Sci 4:2682–2689. https://doi.org/10.1039/c0ee00699h
141. Fei H, Peng Z, Li L et al (2014) Preparation of carbon-coated iron oxide nanoparticles dispersed on graphene sheets and applications as advanced anode materials for lithium-ion batteries. Nano Res 7:1–9. https://doi.org/10.1007/s12274-014-0416-0
142. Ma Y, Ji G, Lee JY (2011) Synthesis of mixed-conducting carbon coated porous γ-Fe_2O_3 microparticles and their properties for reversible lithium ion storage. J Mater Chem 21:13009–13014. https://doi.org/10.1039/c1jm12070k
143. Zhang L, Bin WuH, Lou XW (2014) Iron-oxide-based advanced anode materials for lithium-ion batteries. Adv Energy Mater 4:1–11. https://doi.org/10.1002/aenm.201300958
144. Lin J, Raji ARO, Nan K et al (2014) Iron oxide nanoparticle and graphene nanoribbon composite as an anode material for high-performance li-ion batteries. Adv Funct Mater 24:2044–2048. https://doi.org/10.1002/adfm.201303023
145. Wu X, Hu J, Zhang BW et al (2015) Carbon coated Fe_3O_4 nanospindles as a superior anode material for lithium—ion batteries carbon coated Fe_3O_4 nanospindles as a superior anode material for lithium-ion batteries. J Power Sources 259:92–97. https://doi.org/10.1002/adfm.200801386
146. Zeng Z, Zhao H, Wang J et al (2014) Nanostructured Fe_3O_4@C as anode material for lithium-ion batteries. J Power Sources 248:15–21. https://doi.org/10.1016/j.jpowsour.2013.09.063
147. Wu Y, Wei Y, Wang J et al (2013) Conformal Fe_3O_4 sheath on aligned carbon nanotube scaffolds as high-performance anodes for lithium ion batteries. Nano Lett 13:818–823. https://doi.org/10.1021/nl3046409
148. He C, Wu S, Zhao N et al (2013) Carbon-encapsulated Fe_3O_4 nanoparticles as a high-rate lithium ion battery anode material. ACS Nano 7:4459–4469. https://doi.org/10.1021/nn401059h

149. Su Y, Li S, Wu D et al (2012) Two-dimensional carbon-coated graphene/metal oxide hybrids for enhanced lithium storage. ACS Nano 6:8349–8356. https://doi.org/10.1021/nn303091t
150. Hong J, Wang Y, He G, He M (2012) A new approach to $LiFePO_4$/C synthesis: the use of complex carbon source without ball milling. Mater Chem Phys 133:573–577. https://doi.org/10.1016/j.matchemphys.2012.01.090
151. Huang X, Du Y, Qu P et al (2017) Effect of carbon coating on the properties and electrochemical performance of $LiFePO_4$/C composites by vacuum decomposition method. Int J Electrochem Sci 12:7183–7196. https://doi.org/10.20964/2017.08.77
152. Chen H, Chen Y, Gong W et al (2011) Preparation and electrochemical performance of LiFePO4/C composite with network connections of nano-carbon wires. Mater Lett 65:559–561. https://doi.org/10.1016/j.matlet.2010.11.012
153. Huang B, Zheng X, Fan X et al (2011) Enhanced rate performance of nano-micro structured $LiFePO_4$/C by improved process for high-power Li-ion batteries. Electrochim Acta 56:4865–4868. https://doi.org/10.1016/j.electacta.2011.02.118
154. Yao Y, Qu P, Gan X et al (2016) Preparation of porous-structured $LiFePO_4$/C composite by vacuum sintering for lithium-ion battery. Ceram Int 42:18303–18311. https://doi.org/10.1016/j.ceramint.2016.08.158
155. Ji L, Toprakci O, Alcoutlabi M et al (2012) α-Fe_2O_3 nanoparticle-loaded carbon nanofibers as stable and high-capacity anodes for rechargeable lithium-ion batteries. ACS Appl Mater Interfaces 4:2672–2679. https://doi.org/10.1021/am300333s
156. Cherian CT, Sundaramurthy J, Kalaivani M et al (2012) Electrospun α-Fe_2O_3 nanorods as a stable, high capacity anode material for Li-ion batteries. J Mater Chem 22:12198–12204. https://doi.org/10.1039/c2jm31053h
157. Wang L, Yu Y, Chen PC et al (2008) Electrospinning synthesis of C/Fe_3O_4 composite nanofibers and their application for high performance lithium-ion batteries. J Power Sources 183:717–723. https://doi.org/10.1016/j.jpowsour.2008.05.079
158. Qin X, Zhang H, Wu J et al (2016) Fe_3O_4 nanoparticles encapsulated in electrospun porous carbon fibers with a compact shell as high-performance anode for lithium ion batteries. Carbon N Y 87:347–356. https://doi.org/10.1016/j.carbon.2015.02.044
159. Wang HG, Zhou Y, Shen Y et al (2015) Fabrication, formation mechanism and the application in lithium-ion battery of porous Fe_2O_3 nanotubes via single-spinneret electrospinning. Electrochim Acta 158:105–112. https://doi.org/10.1016/j.electacta.2015.01.149
160. Kim C, Yang KS, Kojima M et al (2006) Fabrication of electrospinning-derived carbon nanofiber webs for the anode material of lithium-ion secondary batteries. Adv Funct Mater 16:2393–2397. https://doi.org/10.1002/adfm.200500911
161. Te Peng Y, Lo CT (2015) Effect of microstructure and morphology of electrospun ultrasmall carbon nanofibers on anode performances for lithium ion batteries. J Electrochem Soc 162:A1085–A1093. https://doi.org/10.1149/2.0061507jes
162. Chen M, Zhao E, Yan Q et al (2016) The effect of crystal face of Fe_2O_3 on the electrochemical performance for lithium-ion batteries. Sci Rep 6:1–9. https://doi.org/10.1038/srep29381
163. Choy KL (2003) Chemical vapour deposition of coatings. Prog Mater Sci 48:57–170. https://doi.org/10.1016/S0079-6425(01)00009-3
164. George SM (2010) Atomic layer deposition: an overview. Chem Rev 110:111–131. https://doi.org/10.1021/cr900056b
165. Leskelä M, Ritala M (2002) Atomic layer deposition (ALD): from precursors to thin film structures. Thin Solid Films 409:138–146. https://doi.org/10.1016/S0040-6090(02)00117-7
166. Anderson J (2013) Fundamentals of fundamentals 5:447–469
167. Thambidurai M, Muthukumarasamy N, Velauthapillai D, Lee C (2013) Synthesis of garland like ZnO nanorods and their application in dye sensitized solar cells. Mater Lett 92:104–107. https://doi.org/10.1016/j.matlet.2012.10.036
168. Baviskar PK, Zhang JB, Gupta V et al (2011) Nanobeads of zinc oxide with rhodamine B dye as a sensitizer for dye sensitized solar cell application. J Alloys Compd 510:33–37. https://doi.org/10.1016/j.jallcom.2011.08.034

169. Wang Y, Cui X, Zhang Y et al (2013) Preparation of Cauliflower-like ZnO Films by chemical bath deposition: photovoltaic performance and equivalent circuit of dye-sensitized solar cells. J Mater Sci Technol 29:123–127. https://doi.org/10.1016/j.jmst.2012.12.019
170. Wang Y, Sun Y, Zhang X et al (2016) Synthesis of 1D porous Fe_2O_3 nanostructures using SiO_2 scaffold towards good lithium storages. Mater Lett 171:125–128. https://doi.org/10.1016/j.matlet.2016.02.012
171. He L, Wang C, Yao X et al (2014) Synthesis of carbon nanotube/mesoporous TiO_2 coaxial nanocables with enhanced lithium ion battery performance. Carbon N Y 75:345–352. https://doi.org/10.1016/j.carbon.2014.04.013
172. Chen WS, Huang DA, Chen HC et al (2009) Fabrication of polycrystalline ZnO nanotubes from the electrospinning of Zn2+/poly(acrylic acid). Cryst Growth Des 9:4070–4077. https://doi.org/10.1021/cg900297q
173. Luo W, Hu X, Sun Y, Huang Y (2011) Electrospinning of carbon-coated MoO_2 nanofibers with enhanced lithium-storage properties. Phys Chem Chem Phys 13:16735–16740. https://doi.org/10.1039/c1cp22184a
174. Mai L, Xu L, Han C et al (2010) Electrospun ultralong hierarchical vanadium oxide nanowires with high performance for lithium ion batteries. Nano Lett 10:4750–4755. https://doi.org/10.1021/nl103343w
175. Li D, Xia Y (2003) Fabrication of titania nanofibers by electrospinning. Nano Lett 3:555–560. https://doi.org/10.1021/nl034039o
176. Xu X, Tan H, Xi K et al (2015) Bamboo-like amorphous carbon nanotubes clad in ultrathin nickel oxide nanosheets for lithium-ion battery electrodes with long cycle life. Carbon N Y 84:491–499. https://doi.org/10.1016/j.carbon.2014.12.040
177. Shang M, Wang W, Yin W et al (2010) General strategy for a large-scale fabric with branched nanofiber-nanorod hierarchical heterostructure: controllable synthesis and applications. Chem A Eur J 16:11412–11419. https://doi.org/10.1002/chem.201000639
178. Luo H, Huang K, Sun B, Zhong J (2014) Strategy to synthesize Fe_3O_4/C nanotubes as anode material for advanced lithium-ion batteries. Electrochim Acta 149:11–17. https://doi.org/10.1016/j.electacta.2014.10.086
179. Cho JS, Hong YJ, Kang YC (2015) Design and synthesis of bubble-nanorod-structured Fe_2O_3 -Carbon nanofibers as advanced anode material for li-ion batteries. ACS Nano 9:4026–4035. https://doi.org/10.1021/acsnano.5b00088
180. Courtel FM, Duncan H, Abu-Lebdeh Y, Davidson IJ (2011) High capacity anode materials for Li-ion batteries based on spinel metal oxides AMn_2O_4 (A = Co, Ni, and Zn). J Mater Chem 21:10206–10218. https://doi.org/10.1039/c0jm04465b
181. Liu Z, Tay SW, Li X (2011) Rechargeable battery using a novel iron oxide nanorods anode and a nickel hydroxide cathode in an aqueous electrolyte. Chem Commun 47:12473–12475. https://doi.org/10.1039/c1cc15022g
182. Cho JS, Park JS, Kang YC (2016) Preparation of hollow Fe_2O_3 nanorods and nanospheres by nanoscale kirkendall diffusion, and their electrochemical properties for use in lithium-ion batteries. Sci Rep 6:1–13. https://doi.org/10.1038/srep38933
183. Zhu S, Chen M, Sun J et al (2016) Novel highly conductive ferroferric oxide/porous carbon nanofiber composites prepared by electrospinning as anode materials for high performance Li-ion batteries. RSC Adv 6:58529–58540. https://doi.org/10.1039/c6ra04090j
184. Im ME, Pham-Cong D, Kim JY et al (2015) Enhanced electrochemical performance of template-free carbon-coated iron(II, III) oxide hollow nanofibers as anode material for lithium-ion batteries. J Power Sources 284:392–399. https://doi.org/10.1016/j.jpowsour.2015.03.024
185. Chen M, Liu J, Chao D et al (2014) Porous α-Fe_2O_3 nanorods supported on carbon nanotubes-graphene foam as superior anode for lithium ion batteries. Nano Energy 9:364–372. https://doi.org/10.1016/j.nanoen.2014.08.011
186. Wu C, Yin P, Zhu X et al (2006) Synthesis of hematite (α-Fe_2O_3) nanorods: diameter-size and shape effects on their applications in magnetism, lithium ion battery, and gas sensors. J Phys Chem B 110:17806–17812. https://doi.org/10.1021/jp0633906

187. Zhu Y, Zhang JC, Zhai J, Jiang L (2006) Preparation of superhydrophilic α-Fe_2O_3 nanofibers with tunable magnetic properties. Thin Solid Films 510:271–274. https://doi.org/10.1016/j.tsf.2005.09.004
188. Zou M, Li J, Wen W et al (2014) Silver-incorporated composites of Fe_2O_3 carbon nanofibers as anodes for high-performance lithium batteries. J Power Sources 270:468–474. https://doi.org/10.1016/j.jpowsour.2014.07.119
189. Manuscript A (2015) Hierarchical $NiFe_2O_4$/Fe_2O_3 nanotubes derived from metal organic frameworks for superior lithium ion battery anode. https://doi.org/10.1039/C5TA00355E
190. Larcher D, Bonnin D, Cortes R et al (2003) Combined XRD, EXAFS, and Mössbauer studies of the reduction by lithium of α-Fe_2O3 with various particle sizes. J Electrochem Soc 150:1643–1650. https://doi.org/10.1149/1.1622959
191. Larcher D, Masquelier C, Bonnin D et al (2003) Effect of particle size on lithium intercalation into α-Fe_2O_3. J Electrochem Soc 150:133–139. https://doi.org/10.1149/1.1528941
192. Liu Y, Huang K, Luo H et al (2014) Nitrogen-doped graphene-Fe_3O_4 architecture as anode material for improved Li-ion storage. RSC Adv 4:17653–17659. https://doi.org/10.1039/c4ra01080a
193. Reddy MV, Subba Rao GV, Chowdari BVR (2013) Metal oxides and oxysalts as anode materials for Li ion batteries. Chem Rev 113:5364–5457. https://doi.org/10.1021/cr3001884
194. Jiang J, Li Y, Liu J et al (2012) Recent advances in metal oxide-based electrode architecture design for electrochemical energy storage. Adv Mater 24:5166–5180. https://doi.org/10.1002/adma.201202146
195. Liu H, Wexler D, Wang G (2009) One-pot facile synthesis of iron oxide nanowires as high capacity anode materials for lithium ion batteries. J Alloys Compd 487:24–27. https://doi.org/10.1016/j.jallcom.2009.08.043
196. Wu MS, Ou YH, Lin YP (2011) Iron oxide nanosheets and nanoparticles synthesized by a facile single-step coprecipitation method for lithium-ion batteries. J Electrochem Soc 158:231–236. https://doi.org/10.1149/1.3527982
197. Liu J, Li Y, Fan H et al (2010) Iron oxide-based nanotube arrays derived from sacrificial template-accelerated hydrolysis: large-area design and reversible lithium storage. Chem Mater 22:212–217. https://doi.org/10.1021/cm903099w
198. Hassan MF, Rahman MM, Guo ZP et al (2010) Solvent-assisted molten salt process: a new route to synthesise α-Fe_2O_3/C nanocomposite and its electrochemical performance in lithium-ion batteries. Electrochim Acta 55:5006–5013. https://doi.org/10.1016/j.electacta.2010.04.006
199. NuLi Y, Zeng R, Zhang P et al (2008) Controlled synthesis of α-Fe_2O_3 nanostructures and their size-dependent electrochemical properties for lithium-ion batteries. J Power Sources 184:456–461. https://doi.org/10.1016/j.jpowsour.2008.03.004
200. Wu XL, Guo YG, Wan LJ, Hu CW (2008) α-Fe_2O_3 nanostructures: inorganic salt-controlled synthesis and their electrochemical performance toward lithium storage. J Phys Chem C 112:16824–16829. https://doi.org/10.1021/jp8058307
201. Railsback JG, Johnston-Peck AC, Wang J, Tracy JB (2010) Size-dependent nanoscale kirkendall effect during the oxidation of nickel nanoparticles. ACS Nano 4:1913–1920. https://doi.org/10.1021/nn901736y
202. Cho JS, Won JM, Lee JH, Kang YC (2015) Synthesis and electrochemical properties of spherical and hollow-structured NiO aggregates created by combining the Kirkendall effect and Ostwald ripening. Nanoscale 7:19620–19626. https://doi.org/10.1039/c5nr05930e
203. Pan JH, Zhang X, Du AJ et al (2008) Self-etching reconstruction of hierarchically mesoporous F-TiO_2 hollow microspherical photocatalyst for concurrent membrane water purifications. J Am Chem Soc 130:11256–11257. https://doi.org/10.1021/ja803582m
204. Chun Zeng H (2007) Ostwald ripening: a synthetic approach for hollow nanomaterials. Curr Nanosci 3:177–181. https://doi.org/10.2174/157341307780619279
205. Lou XW, Wang Y, Yuan C et al (2006) Template-free synthesis of SnO_2 hollow nanostructures with high lithium storage capacity. Adv Mater 18:2325–2329. https://doi.org/10.1002/adma.200600733

206. Takeuchi T, Chimura H, Hamada M, Umezawa H (1975) Controlled porosity by an extreme kirkendall effect. J Antibiot 28:1–21
207. Jeong JM, Choi BG, Lee SC et al (2013) Hierarchical hollow spheres of Fe_2O_3@polyaniline for lithium ion battery anodes. Adv Mater 25:6250–6255. https://doi.org/10.1002/adma.201302710
208. Rahman MM, Wang JZ, Hassan MF et al (2011) Amorphous carbon coated high grain boundary density dual phase $Li_4Ti_5O_{12}$-TiO_2: A nanocomposite anode material for li-ion batteries. Adv Energy Mater 1:212–220. https://doi.org/10.1002/aenm.201000051
209. Wu YP, Rahm E, Holze R (2003) Carbon anode materials for lithium ion batteries. J Power Sources 114:228–236. https://doi.org/10.1016/S0378-7753(02)00596-7
210. Lavela P, Tirado JL (2007) $CoFe_2O_4$ and $NiFe_2O_4$ synthesized by sol-gel procedures for their use as anode materials for Li ion batteries. J Power Sources 172:379–387. https://doi.org/10.1016/j.jpowsour.2007.07.055
211. Bomio M, Lavela P, Tirado JL (2008) Electrochemical evaluation of $CuFe_2O_4$ samples obtained by sol-gel methods used as anodes in lithium batteries. J Solid State Electrochem 12:729–737. https://doi.org/10.1007/s10008-007-0420-3
212. Sharma Y, Sharma N, Rao GVS, Chowdari BVR (2008) Li-storage and cyclability of urea combustion derived $ZnFe_2O_4$ as anode for Li-ion batteries. Electrochim Acta 53:2380–2385. https://doi.org/10.1016/j.electacta.2007.09.059
213. Guo X, Lu X, Fang X et al (2010) Lithium storage in hollow spherical $ZnFe_2O_4$ as anode materials for lithium ion batteries. Electrochem Commun 12:847–850. https://doi.org/10.1016/j.elecom.2010.04.003
214. Kalai Selvan R, Kalaiselvi N, Augustin CO et al (2006) $CuFe_2O_4$/SnO_2 nanocomposites as anodes for Li-ion batteries. J Power Sources 157:522–527. https://doi.org/10.1016/j.jpowsour.2005.07.030
215. NuLi YN, Chu YQ, Qin QZ (2004) Nanocrystalline $ZnFe_2O_4$ and Ag-doped $ZnFe_2O_4$ films used as new anode materials for Li-ion batteries. J Electrochem Soc 151:1–8. https://doi.org/10.1149/1.1760576
216. Fu Y, Chen Q, He M et al (2012) Copper ferrite-graphene hybrid: a multifunctional heteroarchitecture for photocatalysis and energy storage. Ind Eng Chem Res 51:11700–11709. https://doi.org/10.1021/ie301347j
217. Mao J, Hou X, Wang X et al (2015) The cubic aggregated $CoFe_2O_4$ nanoparticle anode material for lithium ion battery with good performance. Mater Lett 161:652–655. https://doi.org/10.1016/j.matlet.2015.08.102
218. Dong Y, Chui YS, Ma R et al (2014) One-pot scalable synthesis of Cu-$CuFe_2O_4$/graphene composites as anode materials for lithium-ion batteries with enhanced lithium storage properties. J Mater Chem A 2:13892–13897. https://doi.org/10.1039/c4ta02203c
219. Xia H, Zhu D, Fu Y, Wang X (2012) $CoFe_2O_4$-graphene nanocomposite as a high-capacity anode material for lithium-ion batteries. Electrochim Acta 83:166–174. https://doi.org/10.1016/j.electacta.2012.08.027
220. Zhang M, Yang X, Kan X et al (2013) Carbon-encapsulated $CoFe_2O_4$/graphene nanocomposite as high performance anode for lithium ion batteries. Electrochim Acta 112:727–734. https://doi.org/10.1016/j.electacta.2013.09.034
221. Li S, Wang B, Liu J, Yu M (2014) In situ one-step synthesis of $CoFe_2O_4$/graphene nanocomposites as high-performance anode for lithium-ion batteries. Electrochim Acta 129:33–39. https://doi.org/10.1016/j.electacta.2014.02.039
222. Zhang Z, Li W, Zou R et al (2015) Layer-stacked cobalt ferrite ($CoFe_2O_4$) mesoporous platelets for high-performance lithium ion battery anodes. J Mater Chem A 3:6990–6997. https://doi.org/10.1039/c5ta00073d
223. Bashir S, Hanumandla P, Huang HY, Liu JL (2018) Nanostructured materials for advanced energy conversion and storage devices: safety implications at end-of-life disposal. Nanostruct Mater Next-Gener Energy Storage Convers Fuel Cells 4:517–542. https://doi.org/10.1007/978-3-662-56364-9_18

224. Tarascon JM, Armand M (2001) Issues and challenges facing rechargeable batteries. Nature 414:359–367. https://doi.org/10.1038/35104644
225. Wang J, King P, Huggins RA (1986) Investigations of binary lithium-zinc, lithium-cadmium and lithium-lead alloys as negative electrodes in organic solvent-based electrolyte. Solid State Ionics 20:185–189. https://doi.org/10.1016/0167-2738(86)90212-2
226. Wang HG, Liu D, Li Y, Duan Q (2016) Single-spinneret electrospinning fabrication of $CoFe_2O_4$ nanotubes as high-performance anode materials for lithium-ion batteries. Mater Lett 172:64–67. https://doi.org/10.1016/j.matlet.2016.02.133
227. Peng S, Li L, Srinivasan M (2014) Electrospun $CuFe_2O_4$ nanotubes as anodes for high-performance lithium-ion batteries. J Energy Chem 23:301–307. https://doi.org/10.1016/S2095-4956(14)60151-0
228. Wu L, Xiao Q, Li Z et al (2012) $CoFe_2O_4$/C composite fibers as anode materials for lithium-ion batteries with stable and high electrochemical performance. Solid State Ionics 215:24–28. https://doi.org/10.1016/j.ssi.2012.03.044
229. Teh PF, Sharma Y, Pramana SS, Srinivasan M (2011) Nanoweb anodes composed of one-dimensional, high aspect ratio, size tunable electrospun $ZnFe_2O_4$ nanofibers for lithium ion batteries. J Mater Chem 21:14999–15008. https://doi.org/10.1039/c1jm12088c
230. Xie W, Li S, Wang S et al (2014) N-doped amorphous carbon coated Fe_3O_4/SnO_2 coaxial nanofibers as a binder-free self-supported electrode for lithium ion batteries. ACS Appl Mater Interfaces 6:20334–20339. https://doi.org/10.1021/am505829v